

Parametric Modeling Investigation of a Radially-Staged Low-Emission Aviation Combustor

Christopher M. Heath*

NASA John H. Glenn Research Center at Lewis Field, Cleveland, OH 44135

Aviation gas-turbine combustion demands high efficiency, wide operability and minimal trace gas emissions. Performance critical design parameters include injector geometry, combustor layout, fuel-air mixing and engine cycle conditions. The present investigation explores these factors and their impact on a radially staged low-emission aviation combustor sized for a next-generation 24,000-lbf-thrust engine. By coupling multi-fidelity computational tools, a design exploration was performed using a parameterized annular combustor sector at projected 100% takeoff power conditions. Design objectives included nitrogen oxide emission indices and overall combustor pressure loss. From the design space, an optimal configuration was selected and simulated at 7.1, 30 and 85% part-power operation, corresponding to landing-takeoff cycle idle, approach and climb segments. All results were obtained by solution of the steady-state Reynolds-averaged Navier-Stokes equations. Species concentrations were solved directly using a reduced 19-step reaction mechanism for Jet-A. Turbulence closure was obtained using a nonlinear κ - ϵ model. This research demonstrates revolutionary combustor design exploration enabled by multi-fidelity physics-based simulation.

Nomenclature

A_3	= inlet combustor cross sectional area, m ²
A_4	= exit combustor cross sectional area, m ²
$\frac{D_{32}}{f/d}$	= Sauter mean diameter, μm fuel to air ratio
\dot{m}_l	= liquid fuel mass flow rate, kg/s
\dot{m}_i	= combustor inlet air mass flow rate, kg/s
\dot{m}_e	= combustor exit mass flow rate, kg/s
M_3	= combustor inlet Mach number
M_4	= combustor exit Mach number
P_3	= combustor inlet pressure, Pa
T_{Fuel}	= initial liquid fuel temperature, K
T_3	= combustor inlet static temperature, K
T_4	= combustor exit static temperature, K
X_l	= pilot recession depth, cm
X_2	= helical-axial vane angle, deg
X_3	= venturi half-angle, deg
ΔP	= combustor air flow pressure loss
η_c	= combustion efficiency
ρ_i	= combustor inlet density, kg/m ³

* Aerospace Engineer, Propulsion Systems Analysis Branch, MS 5-10, AIAA-Member.

I. Introduction

Environmental standards for aviation combined with rising fuel demand call for innovative combustion strategies to improve fuel economy while reducing harmful trace gas emissions. To meet these requirements, aggressive objectives established by NASA’s Environmentally Responsible Aviation project aim to decrease fuel burn along with landing-takeoff (LTO) cycle and cruise nitrogen oxide (NO_x) emissions over 75% by the year 2025[†]. Through a history of collaboration with industry partners, NASA remains dedicated to identifying and advancing research technologies with demonstrated promise toward achieving these programmatic goals.

As part of NASA’s technology portfolio, lean direct injection (LDI) combustion is being explored as a revolutionary strategy to concurrently satisfy program fuel and emission reduction targets. Despite demonstrated potential [1,2], LDI has received limited commercial adoption due to manufacturing complexity, combustor maintenance and operability concerns. Given these challenges, the motivation of this study is to demonstrate a physics-based process for rapidly screening revolutionary combustor architectures suitable for LDI. More broadly, this work investigates how radial fuel staging, pilot flame shielding and injector geometry impact operability of an LDI-capable combustor.

The notional gas-turbine combustor analyzed in this study is sized for an ultra high bypass small-core engine (24,000-lbf thrust class) and incorporates projected technologies and cycle conditions commensurate with a 2030 release date. This includes assumed adoption of material and component technologies to enable appreciable reductions in liner cooling requirements and core size. NASA continues to develop turbofan engine cycles with higher bypass ratios, elevated overall pressure ratios and smaller cores to meet aggressive specific fuel consumption goals. The target vehicle for this engine is the next-generation single aisle transport, expected to supersede the current-era Boeing 737/Airbus A320 class of vehicles over the next 15 years.

To achieve low-emissions and stable performance, radial fuel staging with multiple circuits is leveraged to locally tailor the burning process. At low power loadings, the primary zone is operated at equivalence ratios high enough to ensure flame stability, yet maintain combustion efficiency and limit the production of carbon monoxide and unburned hydrocarbons [3]. Fuel is supplied to secondary zones during mid-power and above operation. Greater fuel distribution at high power loadings enhances combustor uniformity while improving combustion efficiency and decreasing thermal NO_x production.

To quantify the effect of radial fuel staging and injector geometry, this research extends previous work [4] that characterized fundamental swirl-venturi fuel injector operation through a series of steady-state Reynolds-averaged Navier-Stokes (RANS) reacting computations. An additional outcome was the integration of a zero-order thermodynamic engine cycle code with three-dimensional multi-phase Navier-Stokes flow solver. Demonstrating process utility, this investigation adopts a similar software framework, incorporating higher fidelity numerical methods, improved design heuristics, more representative combustor geometry and next-generation cycle conditions. The term fidelity is used in this context to represent the accuracy of the geometry representation in the simulation and level of detail contained in the modeling approach. Simulations involving 0-D or 1-D geometry analyzed at steady-state are considered low fidelity, while 3-D steady-state or transient simulations are considered higher fidelity [5,6]. Robustness of the optimal design in terms of emission performance is also studied by exploring limited part-power operation.

Historically, semi-empirical models combined with experimental data are used to support conceptual gas-turbine combustor development [7,8]. High fidelity simulation is often omitted from conceptual design and reserved for concept refinement and detailed design which yields the following challenges:

- Models derived from experimental observations are limited by the databases from which they were constructed. Leveraging these models constrains new technology development to an evolutionary pathway as revolutionary concepts lie beyond the domain of past knowledge.

[†] Reduction relative to the Civil Aviation Environmental Protection Tier 6 (CAEP/6) standard rule

- Details regarding gas-turbine combustor design and operation remain industry proprietary, dividing the breadth and depth of experimental knowledge between competing parties.
- Traditional design approaches require redundancies to manage the fragmented transition from concept definition to final product. For example, similar geometric definitions of the same concept often coexist at different fidelity levels to suit individual discipline analyst needs. For this reason, bi-directional information is not easily exchanged between groups of differing design scope within an organization.

To overcome these challenges, this study proposes supplementing semi-empirical models frequently used in traditional design with trends from high-fidelity physics-based simulation. The geometric definitions required for high-fidelity analysis can persist through the design process, serving as a repository for information exchange. In this way, the barriers separating conceptual, preliminary and detailed design are significantly reduced yielding a more fluid design approach.

The goals of this research have been realized by characterizing the impact of critical parameters for a next-generation radially staged LDI-capable combustor. Relationships between the reacting combustor aerodynamics, chemistry, engine cycle conditions and geometry have been quantitatively captured. The resulting datasets can be readily applied as a replacement or supplement for historical trends in conceptual design and further exploited to identify optimal candidate combustor architectures. This investigation demonstrates an opportunity for high-fidelity analysis in conceptual design and paves the way for expediting revolutionary low-emission combustor development through physics-based simulation.

II. Lean Direct Injection Combustion

Lean direct injection is an operating mode intended to reduce NO_x and flame temperatures by encouraging uniform combustion approaching the lower flammability limit. LDI was first introduced to address downsides of lean-premixed-prevaporized combustion including autoignition and flashback. A marked feature of LDI is the absence of a quench zone. This means all core air not used for thermal management or liner cooling is devoted to fuel atomization [1, 9]. In LDI, non-premixed liquid fuel is injected directly into the flame zones [10] where near instantaneous burning occurs. Rapid fuel vaporization is critical to achieve a homogeneous reactant mixture, which leads to uniform lean combustion and an attendant reduction in NO_x . At reduced pressures, LDI combustors default to partly premixed operation as reactions occur with some delay giving fuel and air time to naturally premix.

The annular multi-point swirl-venturi combustor studied here contains integrated fuel injector modules that force localized turbulent micro-scale mixing and assist in the fuel atomization process [1]. Figure 1 contains a representative sector of the notional 3-stage combustor dome explored in this study.

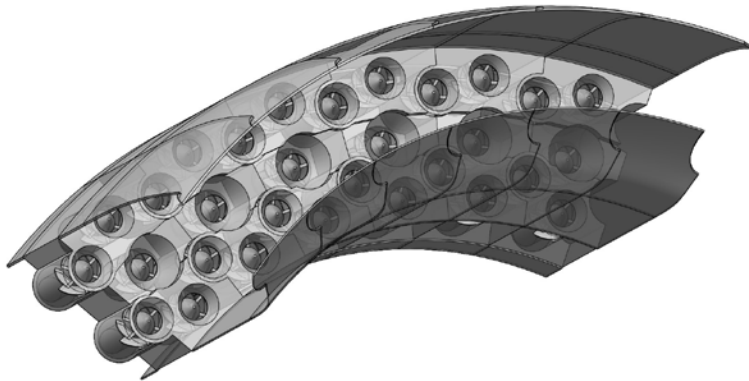


Figure 1. Three-stage multi-point dome sector.

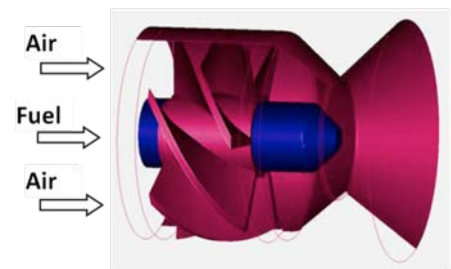


Figure 2. Single LDI module.

For swirl-venturi injection, each injector module is a three-part assembly, comprised of a helical-axial vane set, convergent-divergent venturi and simplex fuel nozzle, which injects finely atomized liquid fuel near the venturi throat. Figure 2 describes a single integrated fuel injector module. The aerodynamic rotation imparted by the helical vanes produces a toroidal core recirculation zone that forms individual flame anchor sites for each injector.

III. Problem Definition

A. Combustor Concept

The combustor concept investigated is an evolution of previous NASA LDI research hardware and intended for higher-pressure environments with expected improvements in operability. The design is an annular three-dome configuration consisting of a central, outer, and inner dome. The central dome houses pilot injectors, while the inner and outer domes contain main injectors utilized for non-idle operation. For this configuration, the central dome may be offset axially to further tailor the combustor flow field and local equivalence ratios for robust operation. For example, a recessed central dome is expected to shield the pilot zone and improve flame stability. The concept assumes radial fuel staging enabled by three separate fuel circuits. At idle, all fuel is shifted to the pilot zone to ensure combustion stability. At high power, the fuel is evenly distributed between the main and pilot injectors to reduce NO_x emissions. All liquid fuel injectors are assumed simplex pressure atomizers. Major differences from prior NASA LDI hardware configurations include more realistic combustor packaging for a small core environment, an increased fuel injector centerbody diameter relative to the air passageway to improve fuel-air mixing, and larger pilot venturi with optional recession intended to enhance stability at low power operation.

Exploiting periodicity, the representative 12-degree sector in Fig. 3 was extracted from the combustor sector in Fig. 1. The sector contains a single pilot injector and four main injectors. The total dome height is 8.89-cm and the inner dome radius is 19.05-cm. The exit venturi diameters of the main and pilot injectors are 2.16-cm and 2.92-cm, respectively. The venturi throat diameter for all injector modules is 1.40-cm.

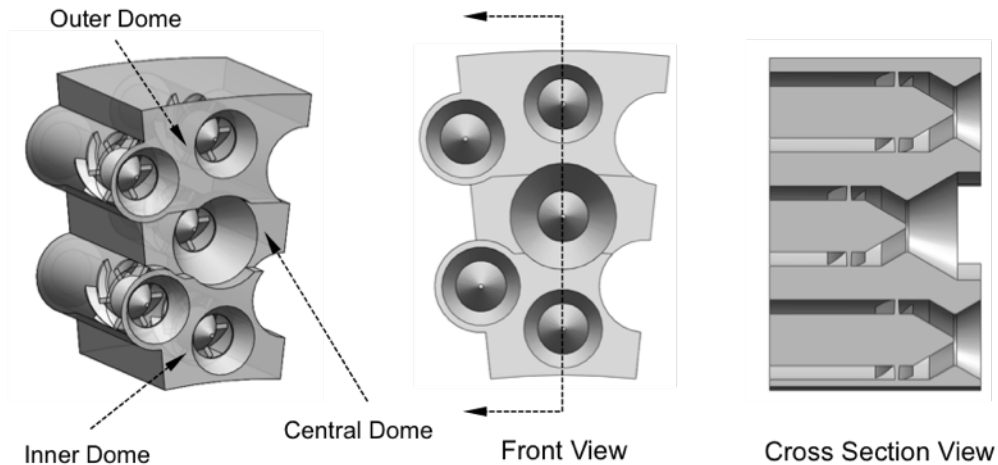


Figure 3. LDI combustor dome definition (12° periodic sector).

The three-dome concept was merged with a straight upstream inlet duct and notional downstream combustor liner as shown in Fig. 4. The total length of the computational domain measured from the upstream entrance to the downstream exit plane is 26.67-cm. Unlike previous research [4], this study simulated effusion cooling through application of a porous boundary condition on the upper and lower surfaces of the combustor liner. Given the assumption of advanced ceramic matrix composites (CMC) and effusion cooling techniques, the amount of core flow dedicated to liner cooling was assumed 15 percent by mass at all operating conditions. This is an aggressive estimate representing an approximate 50 percent reduction in cooling flow requirements over current state-of-the-art combustors.

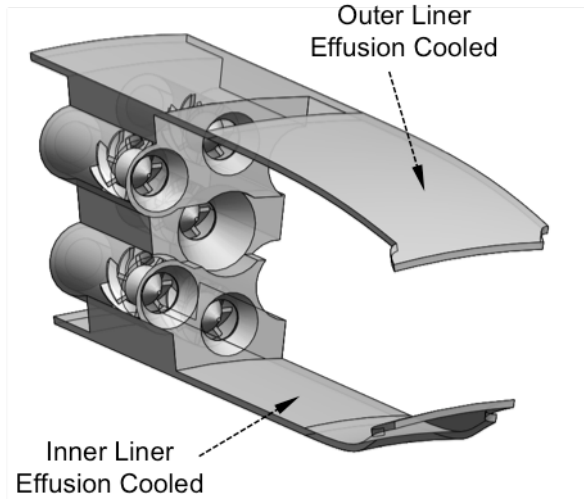


Figure 4. Conceptual LDI combustor model.

B. Design Parameters

A total of three injector module and combustor layout parameters, denoted $X_1 - X_3$, were analyzed. Design parameter X_1 defines the axial offset of the central pilot dome relative to the inner and outer domes. Pilot recession depths between 0.0-cm and 1.91-cm were explored. Figure 5 displays the two extremes, producing flush and fully recessed configurations.

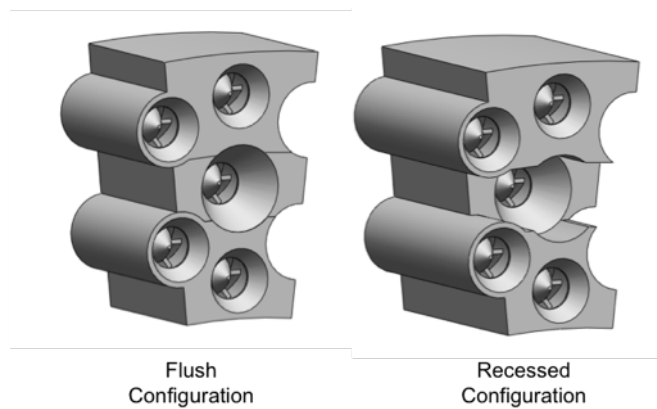


Figure 5. Pilot dome recession definition.

Design parameter X_2 represents the swirl tip angle of the helical-axial vanes for all five injectors. The effect of changing X_2 is demonstrated in Fig. 6 where the overlap between adjacent vanes is constant. Axial swirler height was adjusted to vary vane angle while the revolution of each blade was fixed. A formal definition of vane angle as applied to helical-axial bladed hardware is reported in [11]. Higher vane angles correspond to more rapid flow turning, larger swirl numbers and reduced effective flow areas through the swirler passage.

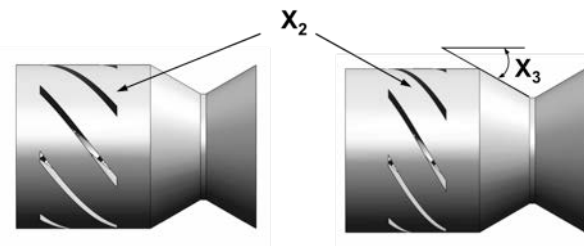


Figure 6: Swirler vane and venturi angle definitions.

Lastly, design parameter X_3 denotes the equivalent converging-diverging half angles of the venturi. Venturi angles were measured as indicated by Fig. 6. The throat and exit diameters of each injector module were held constant, ensuring the dome expansion ratio was identical for all combustor configurations.

In previous research [4], alternate design parameters including injector module diameter and the number of air swirl vanes per injector were explored. In this study, the injector layout, overall combustor dimensions, and injector flow areas were held constant to meet engine thrust requirements. For example, permitting variation of injector diameter introduces a packaging challenge. Either combustor size or the number of air-fuel injector modules would need to vary to achieve tolerable injector airflow rates for stability. Similarly, altering overall combustor size would require significant cycle modifications to maintain thrust and performance requirements. Modifying the number of injector modules would force discrete changes to injector layout. Discrete variations introduce discontinuities in the design space and generally make trends more difficult to identify. There also exists a need to maintain a periodic combustor sector that fits evenly within a full annular combustor. Portions of an injector cannot be modeled due to the non-periodic flow path inside the vane passageway. Within each injector swirler, the number of helical vanes has been set to 7. Prior research [4] found this vane number to produce good flame stabilizing characteristics and recirculation without significant compromise in combustor pressure loss. Basic parameter descriptions and ranges for the design problem formulation are summarized in Table 1.

Design Variable	Description	Range
X_1	Pilot Recession Depth (cm)	$0.0 \leq X_1 \leq 1.91$
X_2	Helical Vane Angle (deg)	$40.0 \leq X_2 \leq 55.0$
X_3	Venturi Half Angle (deg)	$20.0 \leq X_3 \leq 35.0$

Given the design variables and ranges, Table 2 lists the complete set of injector parameter combinations for 15 unique combustor configurations analyzed. The set corresponds to an optimal Latin hypercube [12] design of experiments (DOE).

Design No.	X_1 (cm)	X_2 (deg)	X_3 (deg)
1	0.42	47.12	24.22
2	1.25	42.71	29.84
3	0.30	52.25	23.28
4	0.00	45.27	22.34
5	1.73	53.37	28.91
6	1.85	49.08	30.78
7	0.77	43.28	26.09
8	1.01	44.39	34.53
9	0.54	50.11	33.59
10	0.66	46.18	27.97
11	1.49	51.16	25.16
12	0.89	41.16	20.47
13	0.18	41.92	31.72
14	1.37	54.51	32.66
15	1.61	48.08	21.41

C. Operating Conditions

The engine cycle for this combustor produces up to 24,000-lbf thrust at sea level static conditions. The engine ultra high bypass ratio is 19 and the overall pressure ratio is 42 at cruise. The selected bypass ratio is optimistic, but considered necessary to meet NASA’s goals for future reductions in specific fuel consumption. To accommodate this size of engine, a conventional podded installation may not be feasible. The combustor flow path determined from aeromechanical component design corresponds with the combustor dimensions stated previously. Performing a one dimensional thermodynamic cycle analysis yields the combustor operating conditions listed in Table 3. The LDI concept explored here naturally operates in lean partially premixed mode at the lower pressure conditions.

TABLE 3: Combustor Operating Conditions

Power Setting (%)	T_3 (K)	P_3 (MPa)	\dot{m}_1 (kg/s)	T_4 , target (K)	Liner Cooling (%)
7.1	545.2	0.696	6.62	925.5	15
30	647.9	1.315	10.72	1247.1	15
85	810.6	2.865	19.58	1738.5	15
100	840.9	3.252	21.59	1833.2	15

The upstream combustor total pressure (P_3), total temperature (T_3) and air mass flow rate (\dot{m}_1) were fixed for all simulations by cycle requirements. Note the mass flow rate reported in Table 3 is for the full annular combustor. Only 1/30th of this mass flow was used for simulations, 15% of which was introduced downstream of the injectors through simulated effusion wall cooling. The combustor downstream static pressure (P_4) was varied across the design space to account for total pressure losses unique to each dome configuration. The target combustor exit temperature at full power (T_4) was limited to 1833.17-K as a turbine blade material constraint. The required f/a to achieve this target T_4 was estimated using an adiabatic flame temperature calculation, assuming ideal combustion efficiency. The predicted average exit temperatures also considered thermal losses due to liner cooling with perfect mixing assumed between the cooling flow and primary air streams.

D. Fuel Staging Strategy

The fuel shifting strategy applied for this design includes the three individual circuits labeled in Fig. 7. The pilot circuit independently supplies fuel to the pilot injectors during all phases of operation. The main 1 circuit evenly distributes fuel between the two most centrally located injectors on the outer and inner domes. All fuel was shifted to the main 1 and pilot stage at 30% part power and above. Main 2 injectors were supplied fuel by a separate circuit activated at 75% power and above. Fuel splits between operating stages were kept equal for simplicity and to ensure uniform fuel distribution. Air splits between all injectors were equal, as no mechanism was used to alter or shut off airflow to individual injectors. Under real operation, the pilot would typically have a higher local f/a ratio for added stability. The local injector equivalence ratios are listed in Table 4 for each power setting.

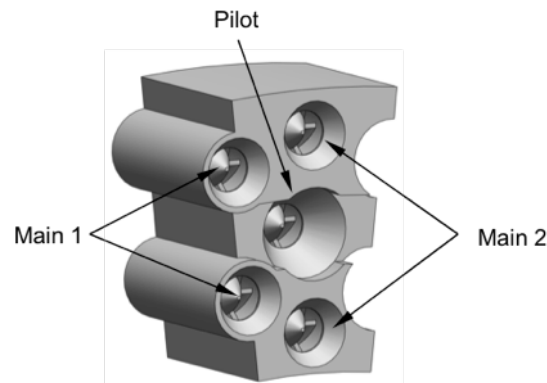


Figure 7. Fuel staging circuits.

Power Setting (%)	ϕ_{Pilot}	$\phi_{\text{Main 1}}$	$\phi_{\text{Main 2}}$
7.1	0.863	0.0	0.0
30	0.484	0.484	0.0
85	0.496	0.496	0.496
100	0.465	0.465	0.465

E. Performance Objectives

The following metrics were used to evaluate the performance of each LDI sector configuration:

1. Overall total pressure loss ($\Delta P/P_3$) across the combustor
2. Predicted nitrogen oxide emission index (E_{INO_x}) measured at the combustor exit plane

In general, combustor efficiency and temperature profile factor are also of significant interest. Given the design exploration was performed at a single operating condition representative of takeoff, combustor efficiencies were found to be exceptionally high with no discernable variation between configurations. Similarly, temperature profile factors were consistent across the design space with differences negligible. For these reasons, combustor efficiency and profile factor were not included as objectives.

IV. Computational Tools, Numerical Methods and Software Integration

A. Geometry Automation

A parametric combustor geometry was developed top-down using the commercial computer-aided design (CAD) package SolidWorks®, with relations driving many free model dimensions. Design parameters were manipulated programmatically by leveraging the SolidWorks application programming interface (API). The positive injector hardware was subtracted from a 12° annular wedge to produce the computational flow domain depicted in Fig. 8. The result was exported to a CAD neutral file format suitable for automated blocking and discretization.

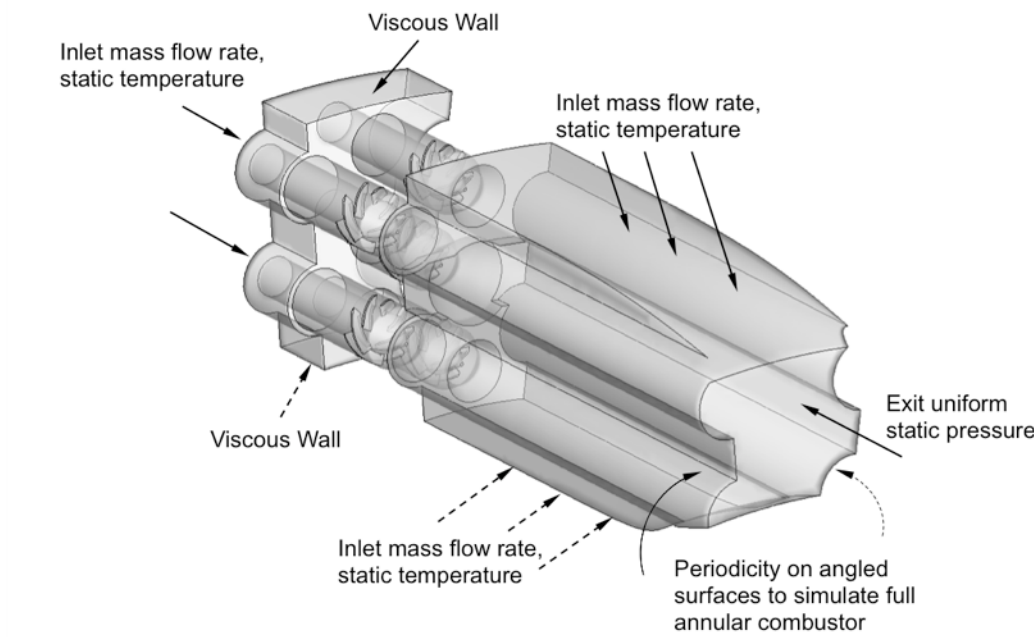


Figure 8. Boundary conditions applied to the computational domain.

B. Mesh Generation

The commercial meshing package Cubit® was used to generate unstructured, multi-block, tetrahedral volume grids for each sector configuration defined in Table 2. A Python-script was used to communicate through the mesh software API, enabling automated geometry import, cleanup, grid generation and boundary surface tagging.

Each block of the domain was individually discretized with constraints controlling the maximum allowable gradient between cells and the maximum and minimum cell size. Each constraint was iteratively relaxed until all cells within each block met an aspect ratio criterion of 6.0 or less. For flows with high swirl and recirculation, cell aspect ratios near unity are desired. All flow domains were meshed with roughly 6 million cells using geometry-based refinement near the injectors to capture boundary and shear-layer effects.

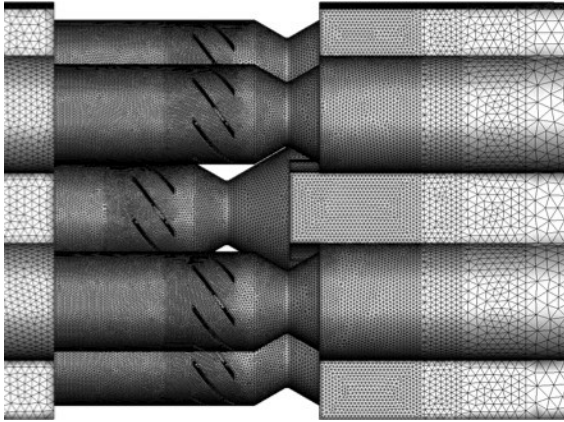


Figure 9. Sample unstructured tetrahedral surface grid near injector region.

Previous grid refinement studies for similar LDI geometries have demonstrated one million tetrahedral elements per injector sufficiently resolves important flow features inside the vane passageways, including static pressure loss when compared to experimental data [13]. Figure 9 displays a typical surface grid near the injector region.

Figure 8 lists the boundary conditions applied to the control volume. Periodic boundaries were specified on either angled side of each sector to simulate the full annular combustor. The upper and lower radial surfaces were assigned viscous wall conditions, enabling wall and confinement effects to be captured. A mass flow rate and static temperature boundary condition was specified at the combustor inlet, along with a turbulence intensity

level of 5% assumed from the high-pressure compressor (HPC) exit. Inlet mixing lengths were assumed 30 percent of the flow passage height (approximately 3.048-cm). A farfield static pressure boundary condition was prescribed at the downstream exit surface. An inlet mass flow and static temperature boundary condition was also prescribed on the combustor liner walls. Mass flow was distributed uniformly over the effusion-cooled surfaces with velocity specified in the surface normal direction. External surfaces not explicitly specified in Fig. 8, including the fuel nozzle, swirl vanes, and venturi, were assigned viscous adiabatic wall conditions.

B. Low-Fidelity Combustor Modeling

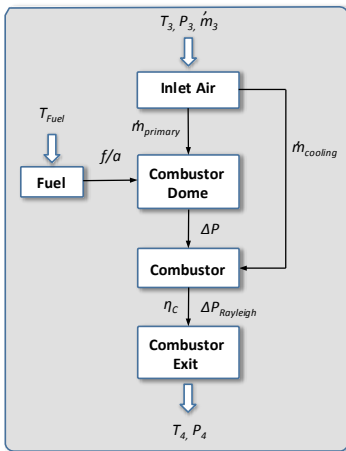


Figure 10. Block diagram of NPSS model used to estimate CFD boundary conditions.

The Numerical Propulsion System Simulation (NPSS) [14] is a component-based zero-order thermodynamic cycle analysis code that has become an industry standard for steady-state engine simulation. With an object-oriented structure, NPSS contains a library of predefined components which may be linked to model many thermodynamic processes.

By combining several computational elements from the NPSS standard library, an isolated zero-order combustor model was developed. Model execution solved for steady-state mass flow rates and all undefined state variables at the entrance and exit of each NPSS flow element. Outputs were supplied as boundary conditions for initializing all computational fluid dynamic (CFD) simulations. The NPSS model also determined the appropriate f/a to achieve the target T_4 at design. Figure 10 is a diagram of the NPSS model including basic input and output parameters for each element. Within the model, the lower heating value for fuel was assumed 42.85-MJ/kg with ideal combustion efficiency, η_c . Bleed ports were used to extract 15% of the primary inlet air and reintroduce it downstream for liner cooling with the post-combustion products. Cross sectional combustor

entrance and exit areas, A_3 and A_4 , were pre-specified by engine cycle requirements and held constant.

C. High-Fidelity Combustor Modeling

The National Combustion Code (OpenNCC) [15,16] is an open-source Navier-Stokes flow solver tailored for advanced chemistry and unsteady modeling of reacting liquid spray. The solver uses a cell-centered finite-volume method for unstructured grids. An explicit four-stage Runge-Kutta integration scheme numerically advances solutions in pseudo time. Viscous fluxes were computed using 2nd order accurate central-differences with a blended 2nd and 4th order Jameson-Turkel dissipation operator for numerical stability [17,18]. Turbulence closure was obtained using a 3rd order κ - ϵ model with variable C_μ [19]. Previous studies [18,20] have proven the κ - ϵ model adequate and efficient for simulating confined swirling flows typical of gas turbine combustion. A generalized wall function model was applied to resolve near-wall turbulence [21]. The flow solver code base has been extensively validated against a number of experimental datasets for single and multipoint LDI configurations with non-reacting and chemically reacting flows [16,20,22-28]. In a recent study [28], EINO_x comparisons were made between several experimental and simulated LDI configurations at 17 different combinations of pressure drop, temperature, fuel-air ratio and with various fuel staging options. In that validation experiment, all predicted EINO_x values fell within $\pm 30\%$ of experimental observations. Given this study applied a similar modeling approach to [28], comparable errors can be expected. All computations were executed on a high performance computer cluster with 432 Intel Xeon E5-2680v3 cores operating at 2.5-GHz. Wall-times were on the order of 100 hours per combustor configuration, neglecting data transfer and queuing overhead. The overall computational budget for this research approached one million compute hours.

For stability, computations were performed using a staged approach, similar to Refs. [4,22,28]. This means a non-reacting gas phase solution was acquired prior to introducing liquid spray and ignition. Convergence of the multi-phase reacting flow field was subsequently achieved. Each combustor was first analyzed to quasi-steady-state without liquid spray. For non-reacting simulations, solutions were acquired for the governing gas phase equations (continuity, momentum, energy and turbulence). A Courant-Friedrichs-Lewy (CFL) number of 0.8 was used. The 2nd order dissipation coefficients (ϵ^2) were permitted to vary between 1×10^{-3} and 0.2 while 4th order damping coefficients (ϵ^4) were fixed at 0.05. The k_2 constant used to scale the second order dissipation gradient switch was set to 0.5. Non-reacting simulations were terminated after reaching a steady-state global air mass imbalance below 1×10^{-2} for 1000 successive iterations. Global mass imbalance was defined using Eq. (1).

$$m_{i,\#} = \frac{\dot{m}_{i,\#}}{\dot{m}_a} \quad (1)$$

After non-reacting flow field convergence, liquid spray and artificial ignition sources were introduced. OpenNCC couples a Lagrangian liquid spray module [29] with gas phase solver to compute flow, thermal, and transport properties of polydisperse sprays. For all injectors, a three-dimensional hollow cone spray pattern was prescribed with full 70-degree angle and 15-degree cone thickness. Initial fuel injection velocity and Sauter mean diameter (D_{10}) were prescribed from empirical data. The injection parameters are considered reasonable assumptions based on fuel nozzle type, size, and required fuel mass flow rates per injector. Fuel properties were based on an assumed fuel injection temperature of 315-K. Polydisperse spray was initialized using 10 discrete droplet size groups comprising a Gaussian distribution.

Species concentrations were computed directly using the 19-step reduced reaction mechanism for C₁₁H₂₁ (Jet-A) and air reported in Table 5. The Arrhenius rate coefficient for temperature was determined from Eq. (2), where A is the pre-exponential factor, n is the temperature ratio exponent, E is the activation energy, T is the temperature, R is the universal gas constant and T_0 is an absolute reference temperature.

$$k = A \left(\frac{T}{T_0} \right)^n e^{-\frac{E}{RT_0}} \quad (2)$$

This chemistry mechanism was first presented in [13] and optimized to match heat release and emission profiles for NO and CO at 27-atm pressure. NO in the reduced mechanism represents the family of nitrogen oxides including nitric oxide by Zeldovich [30], prompt NO by Fenimore [31] and nitrogen oxide formation through nitrous oxide. Each simulation was considered converged after the average combustor exit temperature stabilized to within $\pm 0.5\%$ for 10,000 successive time steps.

Turbulence-chemistry interaction was not simulated for any of the combustor configurations analyzed. Given the average size of the computational domain, the cost of executing a Monte-Carlo turbulence-chemistry model was considered computationally prohibitive. The additional overhead would deter rapid combustor screening and severely limit the number of configurations analyzed within the design space. Flamelet models were also not applied due to liquid spray complications that require significant lookup table memory overhead. For these reasons, laminar chemistry was considered a practical engineering assumption. It should be recognized that refined combustor analysis during detailed design should incorporate higher-fidelity time-accurate simulations with models that more accurately capture turbulence, related interactions and unsteady effects.

Table 5: Nineteen Step Reduced Chemistry Model

Reaction	A (mol-cm-sec-K)	n	E (cal/mol)
$C_{11}H_{21} + O_2 \rightarrow 11 CH + 10 H + O_2$ GLO/ $C_{11}H_{21}$ 0.8/ GLO/ O_2 0.9/	3.00×10^{13}	0.00	3.10×10^4
$CH + O_2 \leftrightarrow CO + OH$	3.00×10^{11}	0.00	0.00
$CH + O \leftrightarrow CO + H$	3.00×10^{12}	1.00	0.00
$H_2 + O_2 \leftrightarrow H_2O + O$	3.98×10^{11}	2.00	2.80×10^4
$H_2 + O \leftrightarrow H + OH$	3.00×10^{14}	0.00	6.00×10^3
$H + O_2 \leftrightarrow O + OH$	4.00×10^{14}	0.00	1.80×10^4
$CO + OH + O \rightarrow CO_2 + H + O$	2.52×10^{13}	1.85	-2.58×10^2
$CO_2 + H \rightarrow CO + OH$	2.14×10^{12}	0.80	2.59×10^4
$H_2O + O_2 \leftrightarrow 2O + H_2O$	2.57×10^{16}	0.00	1.12×10^5
$CO + H_2O + H_2 \leftrightarrow CO_2 + 2H_2$	5.00×10^8	1.48	-1.00×10^3
$CO + H_2 + O_2 \rightarrow CO_2 + H_2O$	1.30×10^{10}	1.60	-1.00×10^3
$N + O_2 \leftrightarrow NO + O$	1.50×10^7	1.20	1.00×10^4
$N + OH \leftrightarrow NO + H$	5.00×10^{12}	1.40	4.80×10^4
$NO + C_{11}H_{21} + O \rightarrow N + O_2 + C_{11}H_{21}$	3.00×10^{16}	1.00	0.00
$H + N_2O \leftrightarrow N_2 + OH$	1.00×10^{17}	0.00	7.55×10^2
$N_2 + O_2 + O \leftrightarrow N_2O + O_2$	2.00×10^{15}	0.00	3.02×10^2
$N_2 + H_2 + O \leftrightarrow N + NO + H_2$	1.00×10^{16}	0.20	3.02×10^2
$N_2O + O \leftrightarrow 2NO$	1.50×10^{15}	0.00	4.80×10^4
$N_2O + N_2 \leftrightarrow 2N_2 + O$	1.00×10^{13}	0.10	0.00

D. Post-processing

Automated post-processing scripts were developed to generate contour plots of important flow field variables. Additionally, these scripts computed and exported integrated boundary information from each solution. Extracted data included pressure, temperature, turbulent kinetic energy and NO mass fractions. $EINO_x$ was computed assuming all NO within the reduced mechanism combines with a free oxygen radical in the atmosphere to produce NO_2 over extended time scales.

E. Software Integration

The object-oriented software framework OpenMDAO [32] was used to manage the integration and automation of all codes. Benefits included encapsulation of best practices, reduction of man-in-the-loop intervention, software

extensibility and code re-use (i.e. similar combustor configurations can be analyzed extensively with minimal added effort). In addition to software integration support, OpenMDAO provides resource allocation utilities to facilitate execution of simulations over heterogeneous and geographically distributed computing environments. OpenMDAO further assists in managing data transfer, data organization and storage.

The framework contains four built-in software classes, called *Component*, *Assembly*, *Driver* and *Workflow*.

- *Component* instances are objects that perform basic computations. Examples include the NPSS thermodynamic combustor model and OpenNCC flow solver model instances.
- *Driver* instances control process iteration and include solvers, optimizers and DOEs.
- All drivers contain a *Workflow* feature to which OpenMDAO components may be added. The workflow determines and manages implicit component execution order based on data transfer between components.
- *Assembly* instances are container objects in which components, drivers, and other assemblies may be added and linked. Assemblies enable hierarchical model construction and manage data transfer between components. An example includes the bi-directional transfer of boundary condition and pressure loss data between the NPSS and OpenNCC components.

The analysis process in Fig. 11 was defined using the OpenMDAO class paradigm. Objects 1, 4 and 5 are iterative process drivers with independent workflows. All other objects are OpenMDAO components. Driver and component roles were defined as follows:

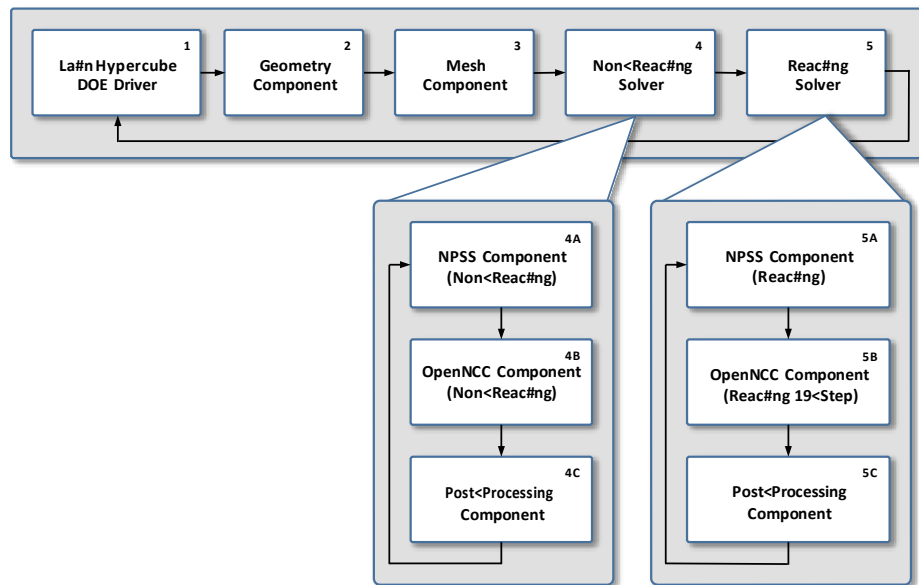


Figure 11: OpenMDAO analysis process for the parametric LDI combustor study.

1) The Latin hypercube DOE driver (1) constructs an optimal Latin hypercube of combustor designs given the set of injector parameters and ranges defined in Table 1. For every combustor configuration, the DOE driver iteratively executes sub-components (2-5) contained in its workflow.

2) The Geometry component (2) launches a CAD application instance, loads a parametric combustor sector model, sets design parameters to match the current DOE case, generates the computational domain and exports the domain to a CAD neutral file.

3) The Mesh component (3) executes remotely by leveraging the OpenMDAO external code interface. The component transfers the computational geometry to a remote compute cluster, launches a background mesh

application instance, loads the recent geometry definition created by Component 2, generates a geometry adaptive mesh, tags boundary surfaces and exports the mesh in a format compatible with the flow solver.

4) For computational efficiency and numerical stability, the non-reacting NPSS model and non-reacting OpenNCC model are first simultaneously converged. This ensures the code assumptions are consistent throughout the solution process and enables gradual convergence of the reacting CFD flowfield. The Non-Reacting driver (4) is a fixed-point solver that iteratively executes sub-components 4A, 4B and 4C until convergence is met. As input, component 4A accepts the geometric cross-sectional area of the current combustor case from component 2,

predefined combustor entrance conditions (T_3, P_3, m_1) and assumes an initial combustor pressure loss. The f/a ratio is set to zero and the NPSS non-reacting component (4A) executes. NPSS performs a zero-dimensional mass and energy balance, computing flow field quantities at the combustor sector inlet and exit boundaries. Output from 4A includes combustor exit pressure, P_4 , which initializes the static pressure exit boundary condition of component 4B. Component 4B (OpenNCC) then executes remotely on a high performance compute cluster. Component functions include managing the writing and transferring of flow solver input files to the compute cluster, executing the job through a batch queuing system and returning all simulation output files to the client host. Once 4B completes, component 4C executes by post-processing OpenNCC results and computing the actual combustor pressure loss. This pressure loss is returned to component 4A and the driver 4 workflow repeats until the predicted combustor pressure losses from NPSS and OpenNCC match within $\pm 0.1\%$. Given each combustor design yields a unique pressure loss based on the geometric configuration, this iteration is necessary to guarantee all configurations are evaluated at identical inflow conditions (T_3, P_3, m_1).

5) Driver 5 is similar to driver 4, but contains a feedback loop that terminates when the average combustor exit temperature, T_4 , reaches steady state. Component 5A accepts as input a target T_4 based on cycle requirements and computes the required f/a assuming full combustion efficiency and equilibrium chemistry. In addition, the combustor pressure drop is adjusted again for Rayleigh pressure losses. Component 5B restarts the gas phase flow solver from the previous non-reacting 4B solution while activating the liquid spray solver and artificial ignition sources. Simulation results are then post-processed by Component 5C to extract flow field data.

V. Results and Discussion

A. Design Space Exploration Results at Takeoff Conditions

Temperature, axial velocity, turbulent kinetic energy and spatial NO mass fraction contours are included in Supplementary Material for all 15 sector configurations at simulated takeoff conditions. For axial cross section views, the zero location is defined at the exit of the pilot venturi. Planar axial slices have been extracted in 5-mm increments upstream and downstream of the zero reference point.

Table 6 summarizes design parameter inputs and objective outputs for each combustor configuration. The effective flow area (AC_d) given by Eq. 3 is also listed.

$$AC_1 = \frac{\dot{m}_1}{\sqrt{\rho_1 V_1}} \quad (3)$$

TABLE 6: Optimal Latin Hypercube Design Matrix Including Objectives

Design No.	X_1 (cm)	X_2 (deg)	X_3 (deg)	$\Delta P/P_3$ (%)	AC_d (in ²)	EINO _x (g/kg)
1	0.42	47.12	24.22	4.56	0.558	17.96
2	1.25	42.71	29.84	4.61	0.555	33.12
3	0.30	52.25	23.28	5.42	0.512	12.89
4	0.00	45.27	22.34	4.04	0.593	24.24
5	1.73	53.37	28.91	6.54	0.466	12.49
6	1.85	49.08	30.78	5.81	0.494	17.47
7	0.77	43.28	26.09	4.34	0.572	26.15

8	1.01	44.39	34.53	4.92	0.537	32.72
9	0.54	50.11	33.59	5.57	0.505	12.90
10	0.66	46.18	27.97	4.71	0.549	19.13
11	1.49	51.16	25.16	5.72	0.498	15.32
12	0.89	41.16	20.47	4.24	0.579	9.45
13	0.18	41.92	31.72	4.20	0.581	36.38
14	1.37	54.51	32.66	6.98	0.451	8.06
15	1.61	48.08	21.41	4.99	0.533	20.86

Figure 12 is a scatter plot matrix describing the relationship between each pair of design parameters and total pressure loss across each combustor configuration. Configuration number labels and ledger lines are included to identify specific designs. All computed pressure losses exceed 4% due to the large bluff body dome surface area inherent in the 3-dome configuration. Figure 12 indicates pressure losses increase primarily with vane angle. This relationship is isolated in Fig. 13 and appears linear where steep vane angles trend with large total pressure losses. A general linear correlation is also provided in Fig. 13. Analysis of spatial turbulent kinetic energy fields indicates high turbulence in the swirl vane passages corresponds with larger pressure losses. This indicates turbulent kinetic energy and viscous effects through the swirler are the primary mechanisms for pressure loss.

A weak positive correlation between pilot recession depth and combustor pressure loss is highlighted in Fig. 14. Recessed configurations contain a larger wetted area downstream of the pilot injector that produces higher viscous forces and decreases total pressure prior to combustion.

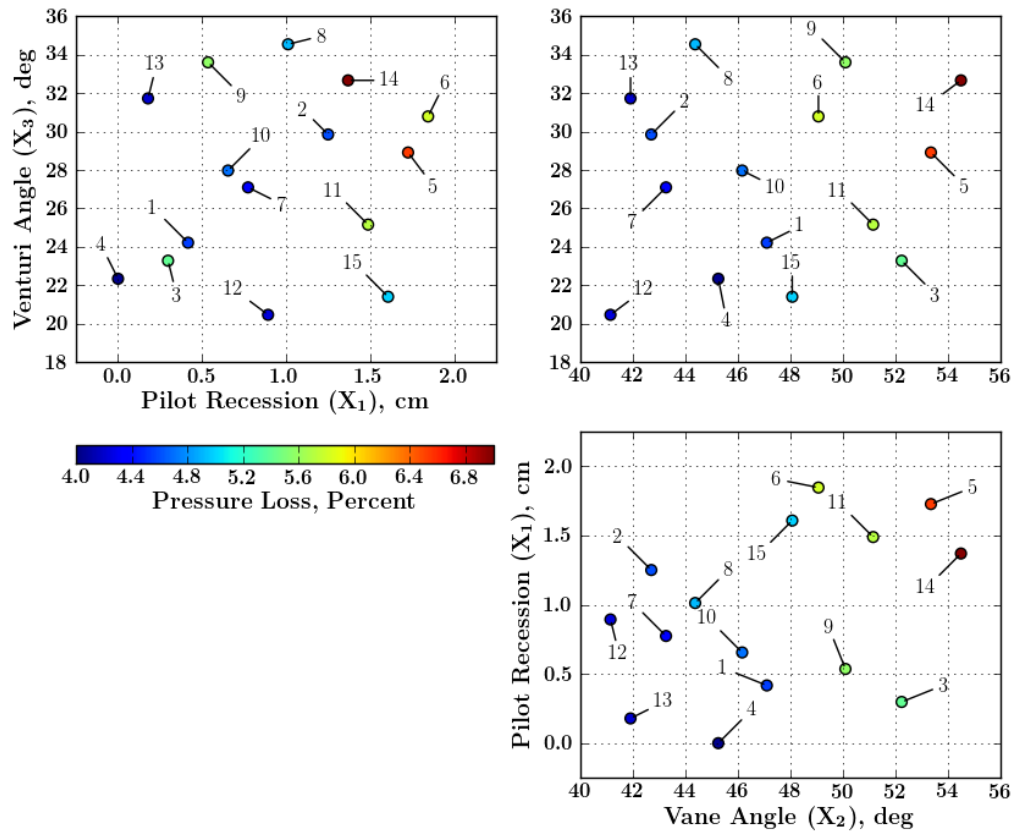


Figure 12: Scatter plot matrix of pressure losses for all 15 combustor configurations.

Figure 15 is a scatter plot matrix containing the response variable $EIXO_x$ versus each pair of geometric design parameters for all 15 combustor configurations. As shown in the upper right plot of Fig. 15, designs with shallow swirl vane angles combined with large venturi turning produce highest NO_x concentrations.

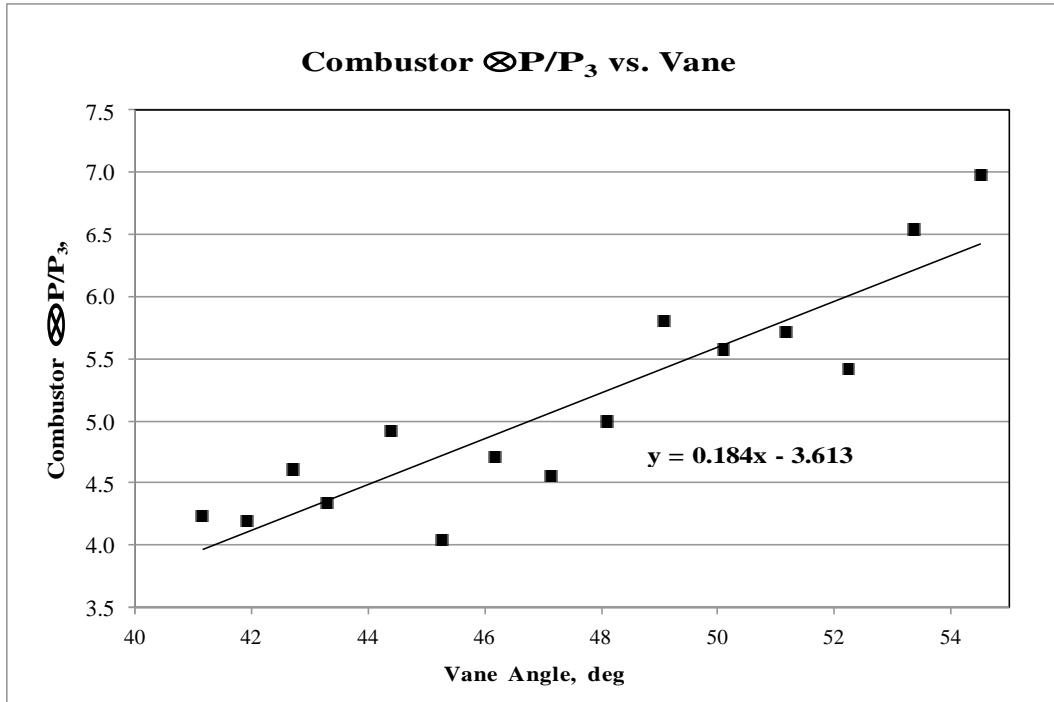


Figure 13: Partial relationship between combustor pressure loss and helical vane angle.

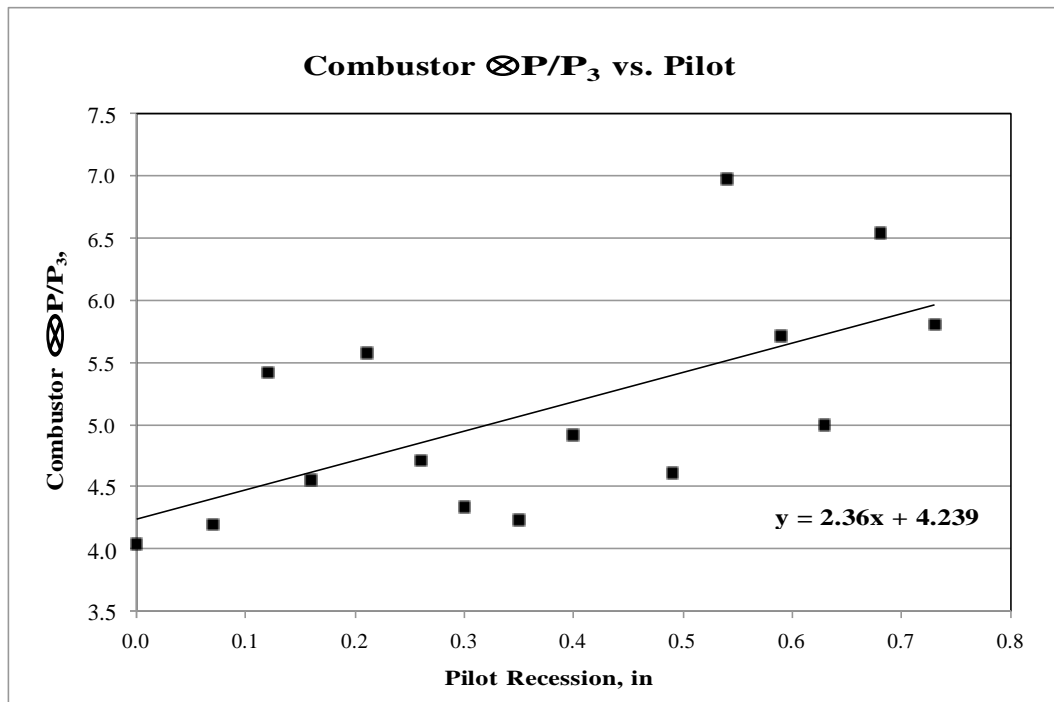


Figure 14: Partial relationship between combustor pressure loss and pilot recession.

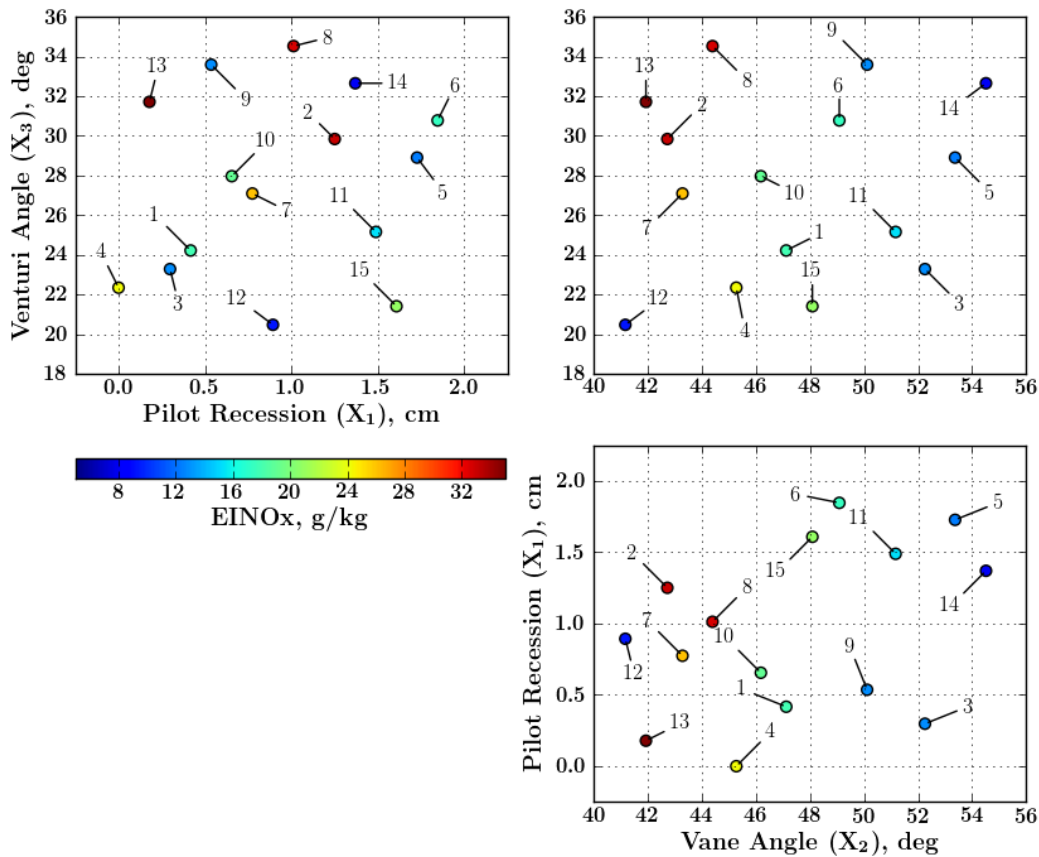


Figure 15: Scatter plot matrix of EINO_x for all 15 combustor configurations.

Figure 16 highlights the partial relationship between EINO_x and helical vane angle. Shallow vane angles were found to produce poor recirculation characteristics, in general. Configurations 7, 4 and 12 suggest emission performance for low swirl designs may be recovered by reducing venturi turning angles. Consulting Fig. 17, recirculation zone strength and size can be inferred from the magnitude and volume of the low axial velocity region downstream of each injector. These contours suggest recirculation zone uniformity across all injectors is a better indicator of EINO_x production than vane angle alone. Qualitatively, configurations where pilot and main injector recirculation zone volume and strength are uniform produce lowest EINO_x values. Similarly, configurations with greatest discrepancy between pilot and main injector recirculation zone flow structures (strength and size) produce highest NO_x concentrations. This trend is maintained throughout the design space, indicating axial velocity contours are a better indicator of combustion flow field uniformity, which in turn correlates with NO_x production. The general axial velocity field of configuration 12 markedly differs from all other designs in that it contains no reverse flow downstream of the pilot or main injectors. Even without recirculation evident at the high power condition, the flow is slowed sufficiently to support flame attachment. More qualitative comparisons can be made using the full dataset included as Supplementary Material.

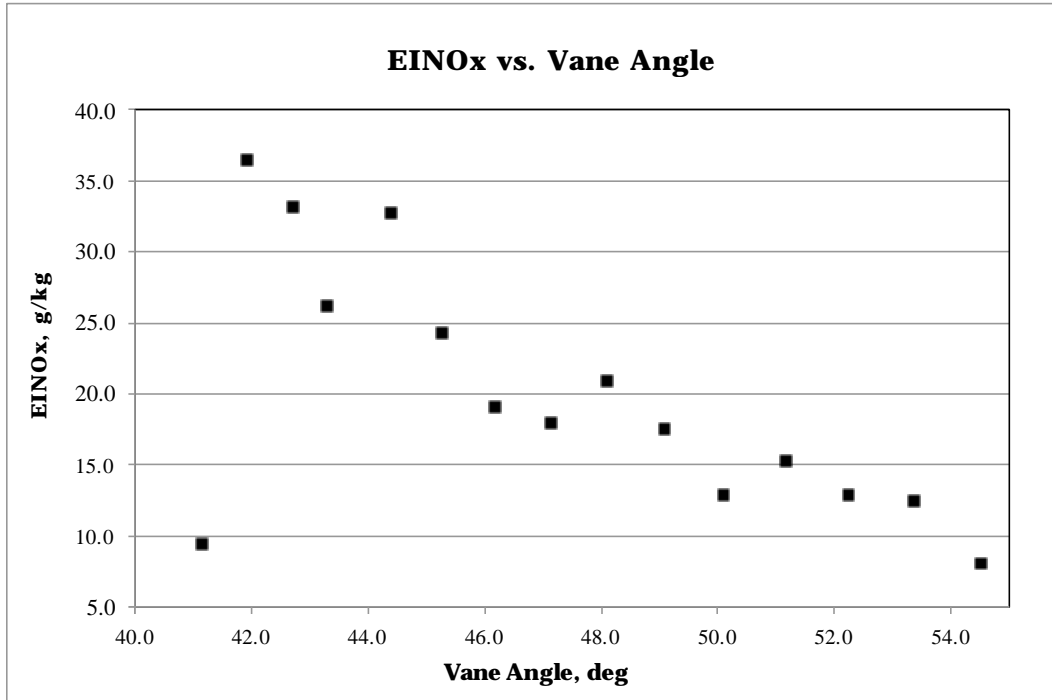


Figure 16: Partial relationship between EINO_x and helical vane angle.

Data also reveals vane angle is not a sole indicator of swirl or recirculation zone intensity. The venturi section yields reduced axial velocities, which promotes recirculation strength. However, excessive convergent-divergent venturi angles can trigger airflow separation and break down of recirculating flow structures.

The partial relationship between EINO_x and venturi angle is plotted in Fig. 18. Overall, a weak positive association between EINO_x and venturi angle is present, where shallow converging-diverging angles trend with lower EINO_x observations on average.

Analysis of local NO mass fractions indicate the main injectors are the primary NO_x sources. For example, a subset of the design space is shown in Fig. 19 with complete data set provided as Supplementary Material. Typical low NO mass fraction concentrations observed directly downstream of the pilot injectors are attributed to reduced pilot flame temperatures. From design intent, the pilot injectors in each configuration have an expanded venturi exit. This feature was intended to promote stronger pilot flow recirculation and stability for idle operation. This also means the pilot has a larger expansion ratio. This increased expansion yields a larger, low-pressure zone inside the pilot cup, resulting in lower flame temperatures and less O₂ and N₂ dissociation. Pilot flames tend to burn more rapidly as the pilot zones contain lower momentum flow, keeping the reacting constituents close to the injection site. The pilot also provides a portion of vaporization energy to the main injectors, as pilot burning occurs upstream of the main 1 and 2 injectors. After the liquid fuel has vaporized, the temperature fields reveal turbulent diffusion flames that become well mixed and uniform by the combustor exit. Sample temperature fields for the first three configurations are shown in Fig. 20 with all configurations included as Supplementary Material.

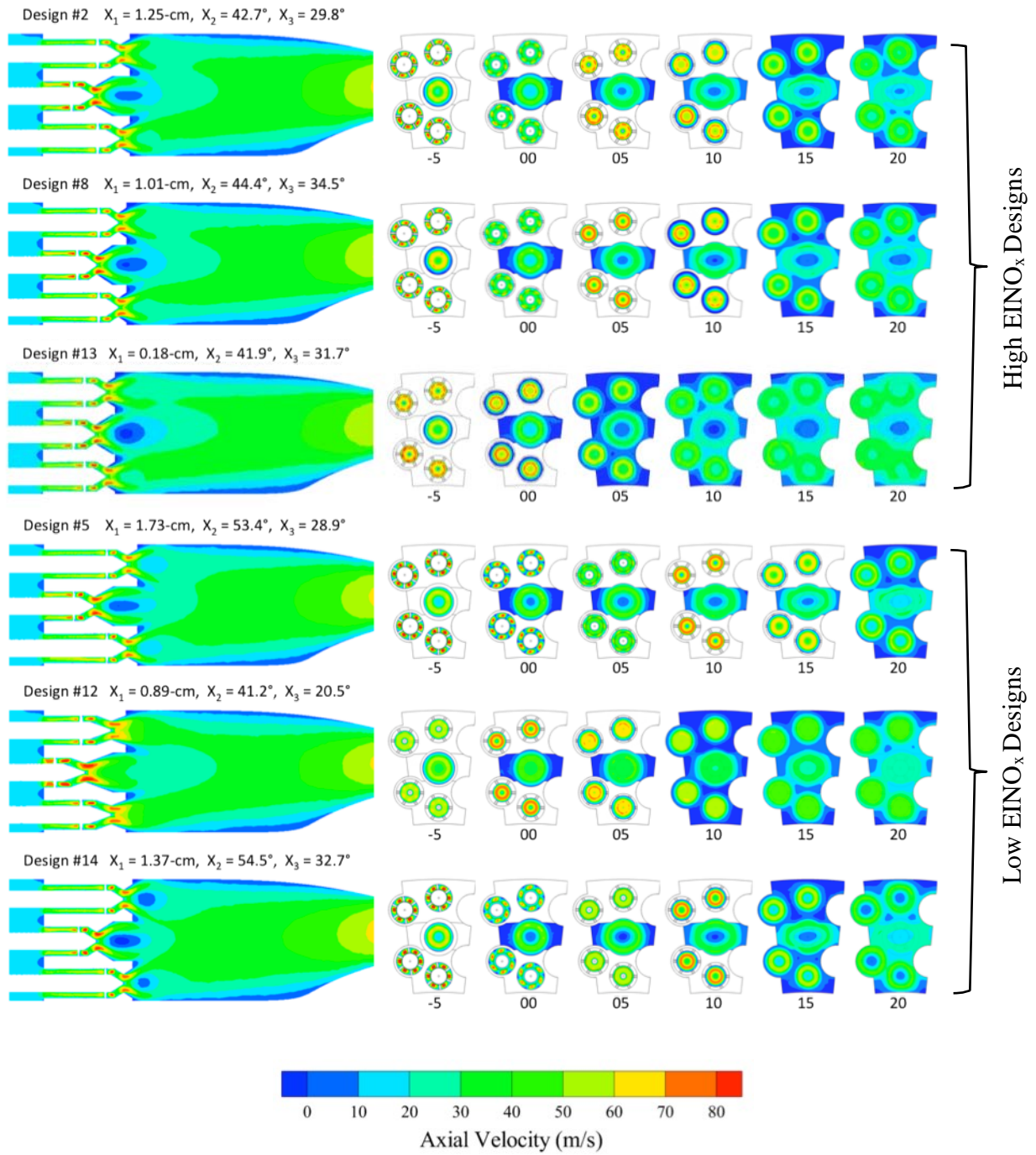


Fig. 17. Reacting axial velocity contours for lowest and highest $EINO_x$ producing configurations.

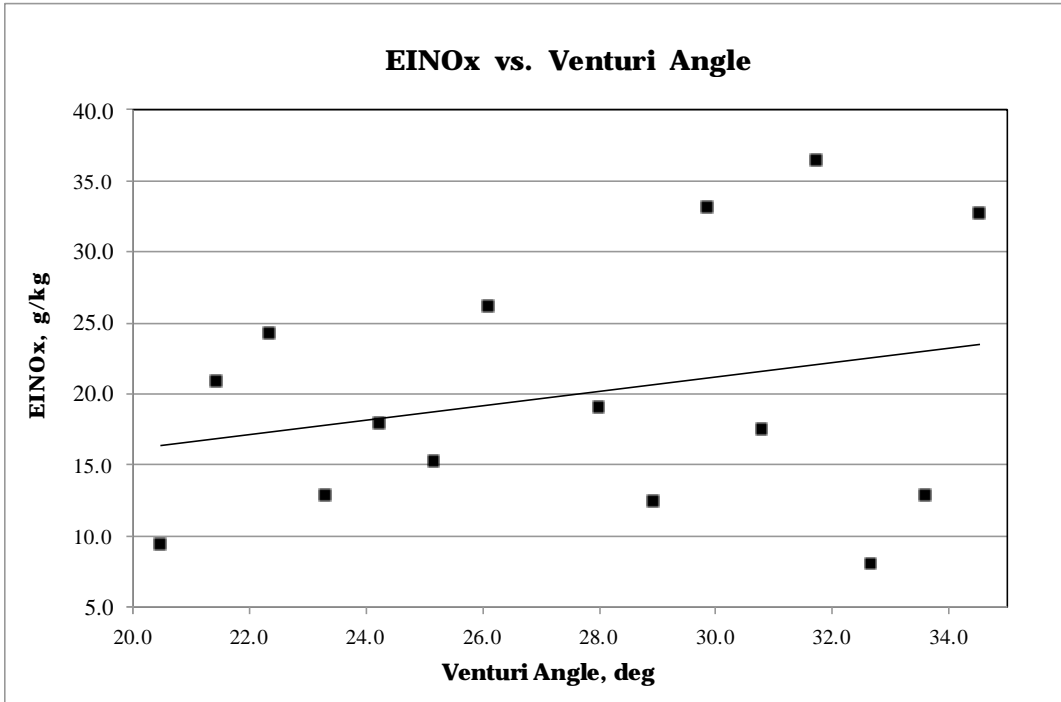


Figure 18: Partial relationship between EINO_x and venturi angle.

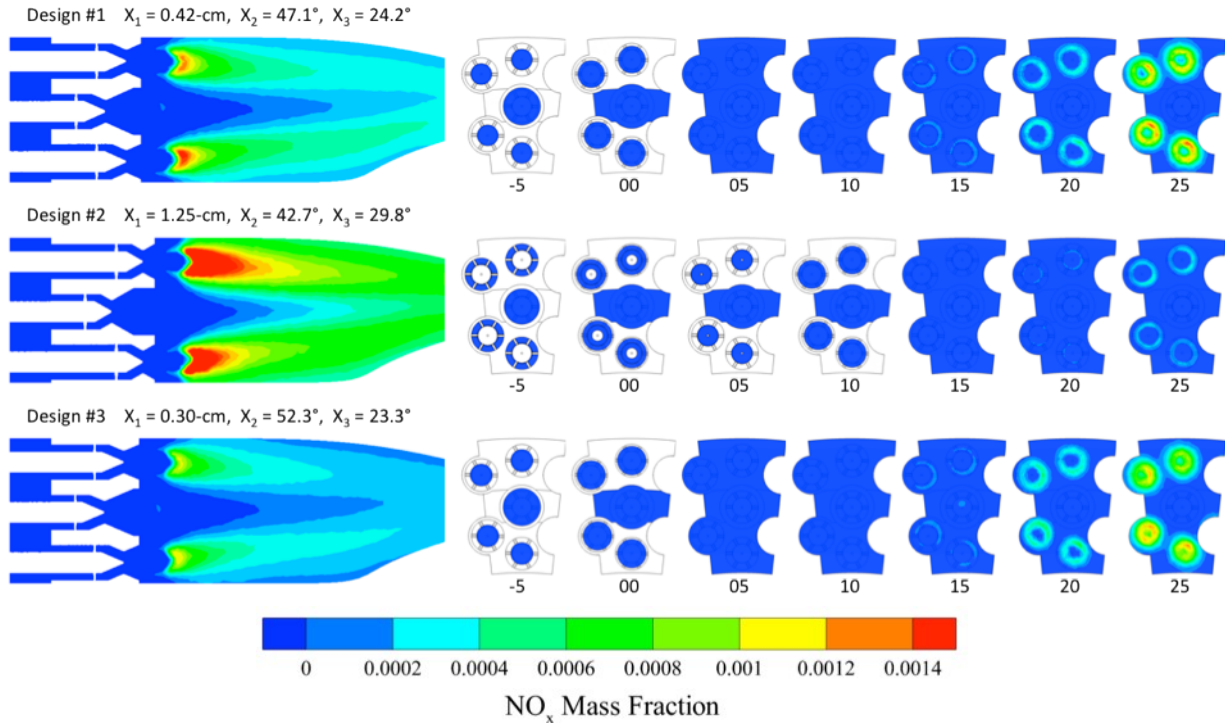


Fig. 19. NO species mass fraction contours for configurations 1-3. NO predominantly forms downstream of the burning zones and is substantially lower near the pilot flames.

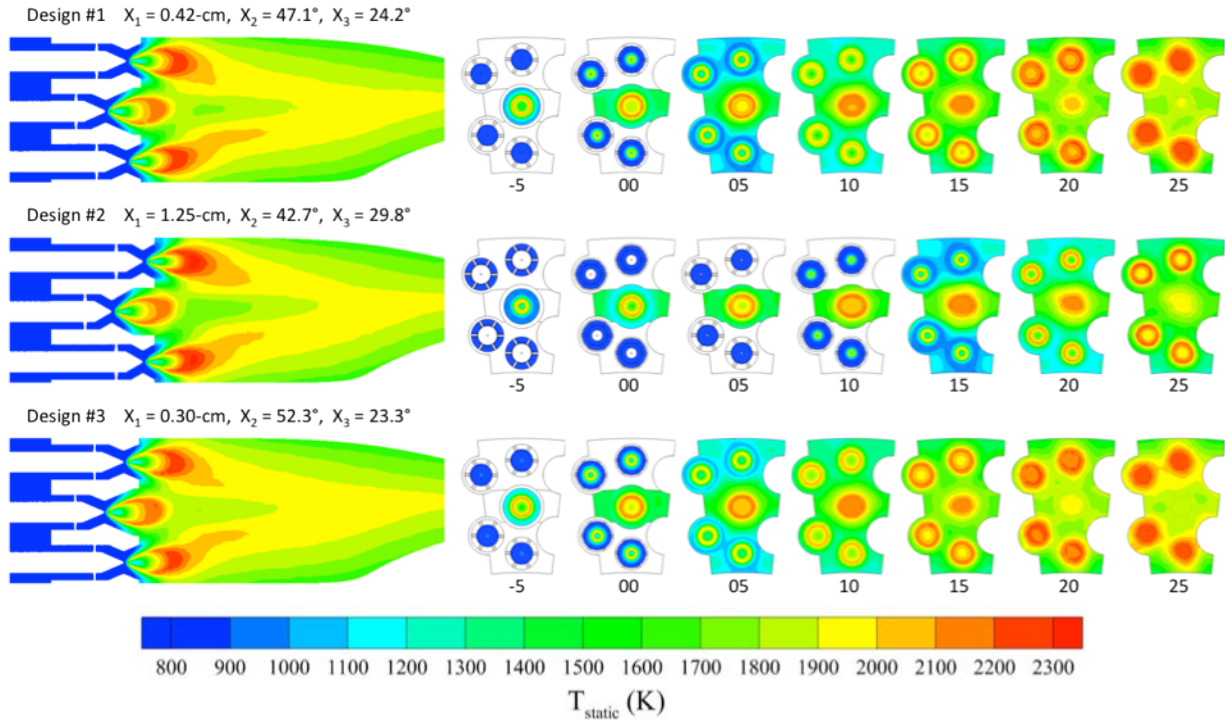


Fig. 20. Temperature contours for configurations 1-3. All designs exhibit stable attached flames. Pilot flame zones are typically reduced in size and exhibit less internal temperature variation.

Reacting liquid fuel spray patterns for each configuration were also computed and included in Supplementary Material. Configurations with weaker recirculation zones and higher axial velocities near the liquid fuel injectors exhibit narrow spray cone angles. Overall, liquid droplets were observed to track well with the axial velocity fields. Designs with uniform recirculation contain more uniform spray cone patterns, which qualitatively trend with lower NO_x production. Often, the pilot liquid fuel droplets evaporate more rapidly than fuel injected through main 1 and 2 fuel circuits. This rapid pilot fuel vaporization is consistent with the higher burning efficiency and lower NO_x concentrations observed.

By analyzing the objective space in Fig. 21, candidate 12 can be readily identified as a desirable combustor that simultaneously yields low NO_x emissions without significant compromise in pressure loss. For these reasons, configuration 12 was selected from the screening process as an optimal combustor warranting further off-design evaluation.

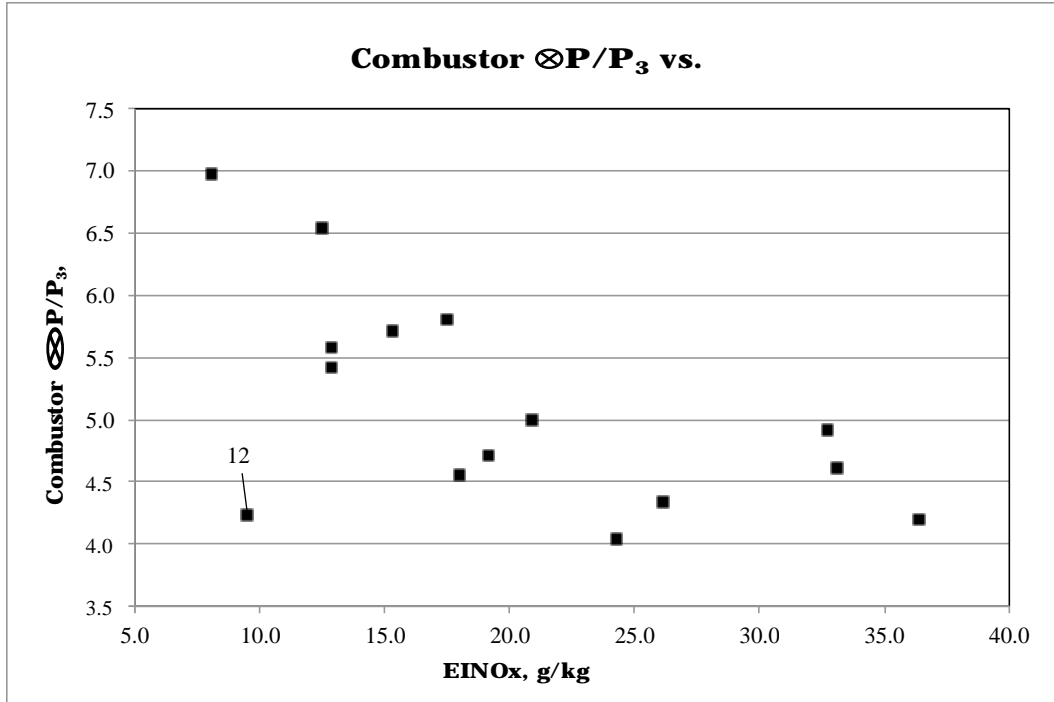


Figure 21: Objective space indicating tradeoff between pressure loss and EINO_x.

B. Off-design Analysis

In addition to high power operation and emission production, operability is also critical for combustor performance. This section characterizes part-power operation of configuration 12 to gauge overall robustness throughout the flight envelope. Three additional simulations were conducted by adjusting the boundary conditions to correspond with the 7.1, 30 and 85% power settings from Table 3. Fuel staging was also introduced as per the strategy outlined in Table 4.

Figures 22 through 26 contain contour plots of temperature, axial velocity, NO mass fraction, turbulent kinetic energy, and liquid fuel spray distributions, respectively. The most noticeable changes occur in the fuel cone spray patterns, which become highly compressed at the 85 and 30% part-power conditions. Once all fuel is shifted to the pilot injector at 7.1% power, liquid spray droplets persist further downstream as combustion occurs at a slower rate. NO mass fractions decline rapidly below the 85% part-power condition, driven by a strong pressure and temperature dependence.

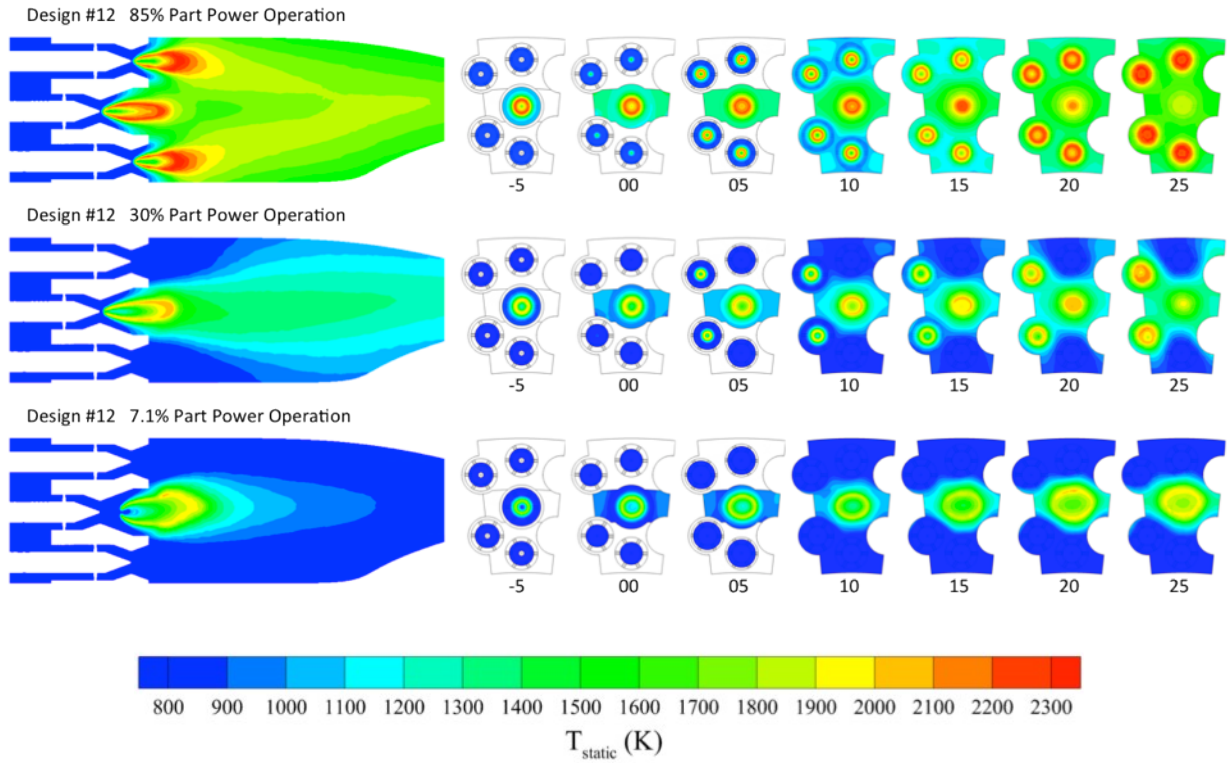


Fig. 22. Temperature contours for part-power operation. Fuel staging strategy demonstrated for each off-design condition.

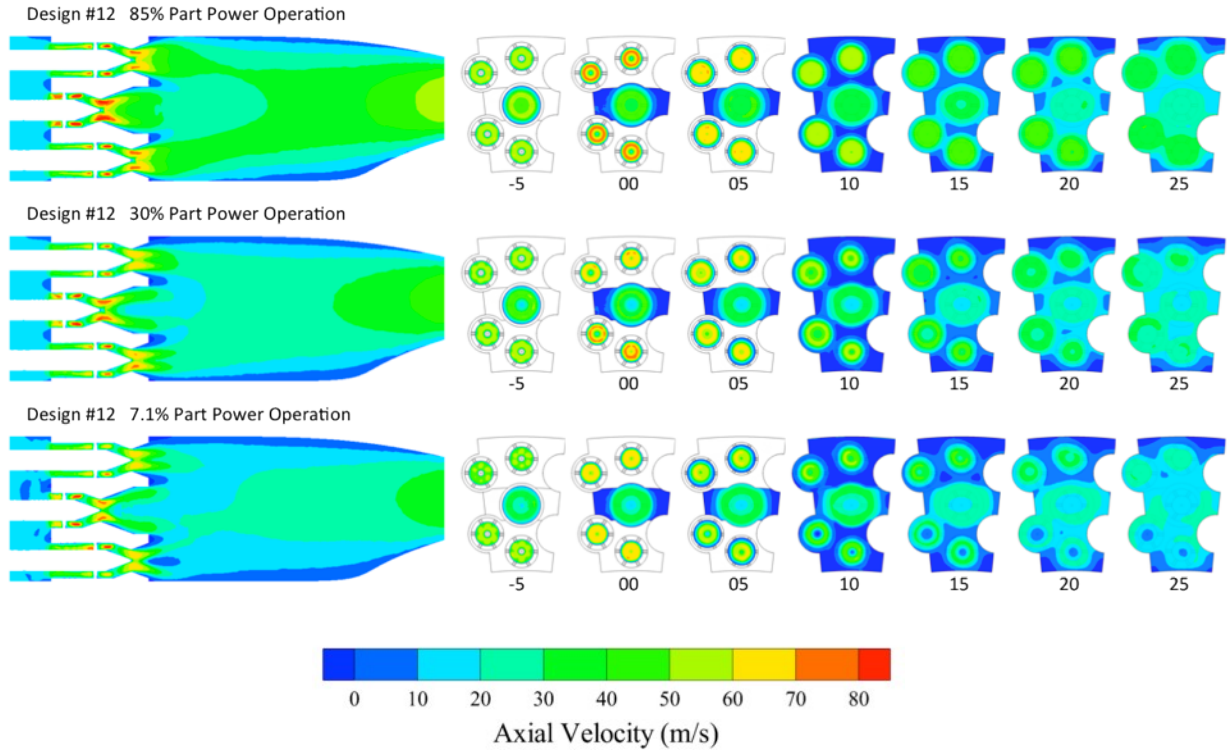


Fig. 23. Axial velocity contours for part-power operation. Axial velocity decreases with reduced power.

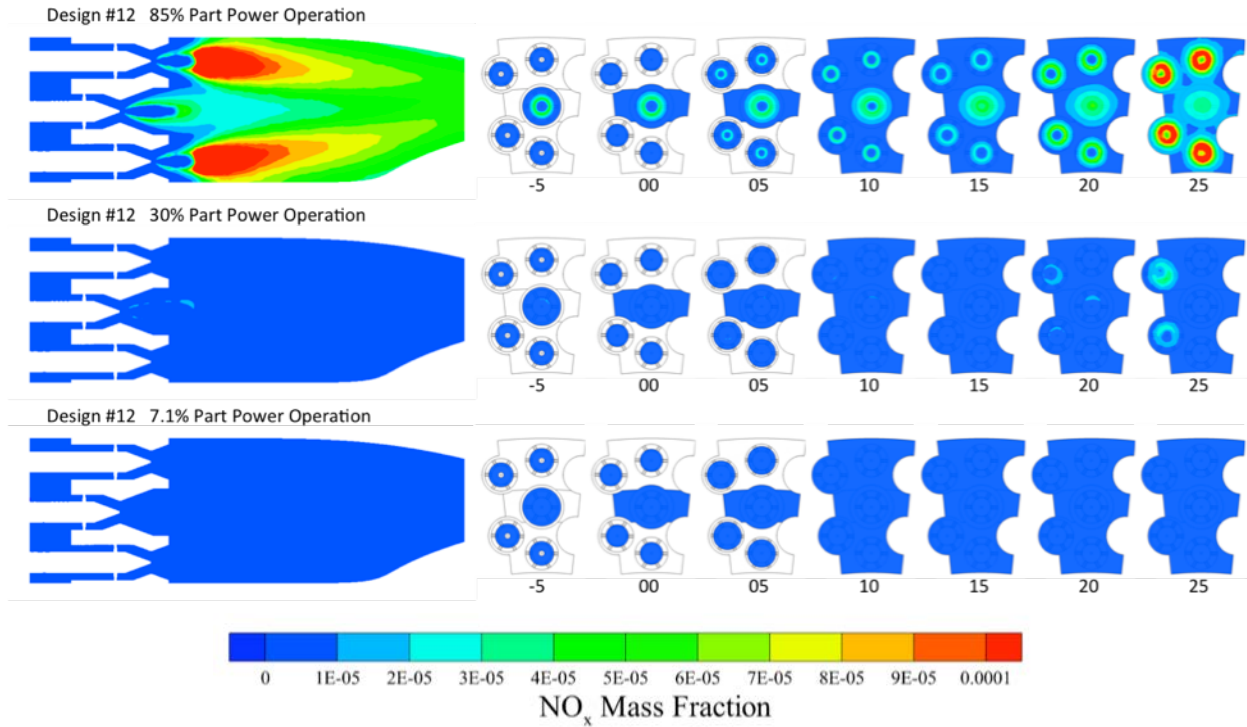


Fig. 24. NO species mass fraction contours for part-power operation. NO concentrations are observed to decline rapidly below the 85% part-power condition.

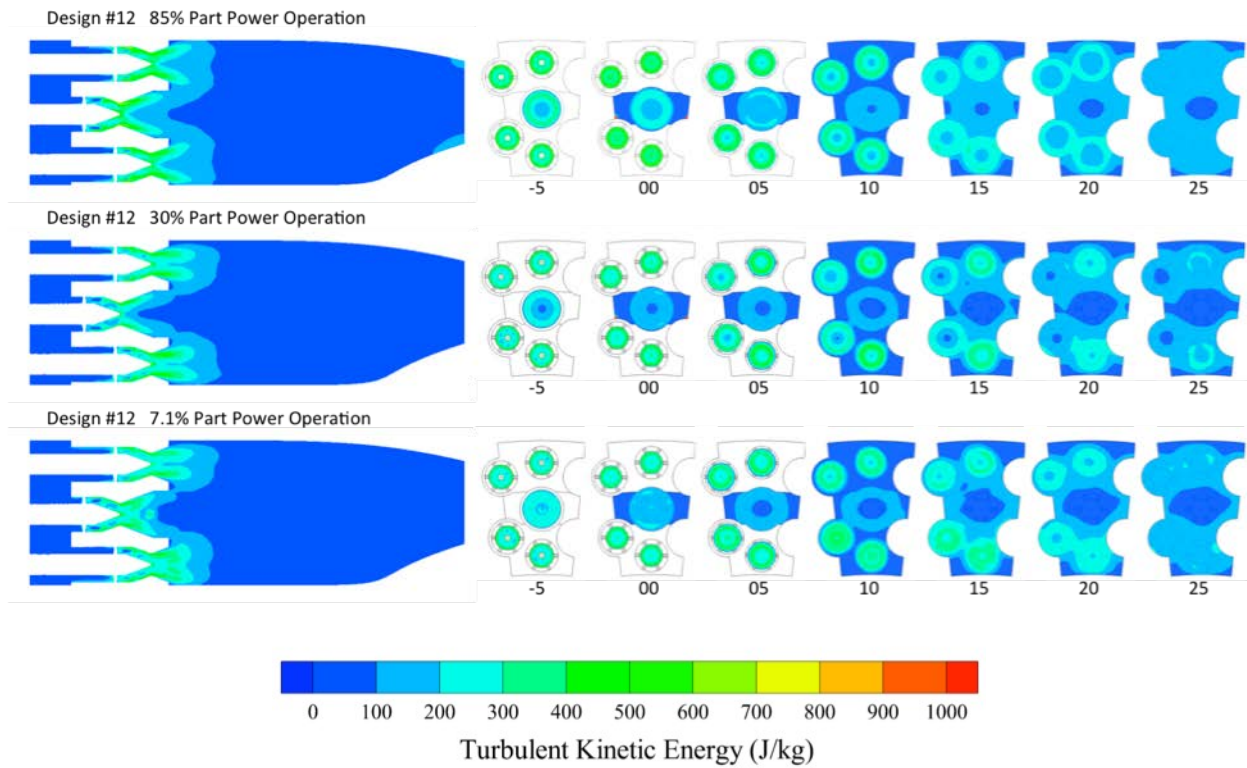


Fig. 25. Turbulent kinetic energy contours for part-power operation. TKE levels remain fairly consistent during off-design operation.

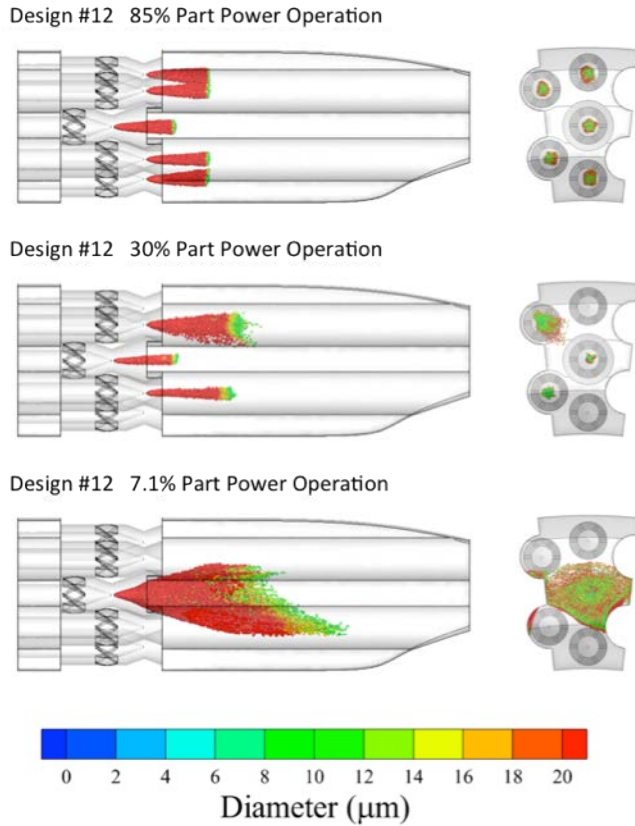


Fig. 26. Reacting liquid spray patterns for part-power operation. At 85% and 30% part-power, the spray cone angle becomes increasingly compressed. Evaporation is delayed with liquid spray persisting furthest into the domain at the 7.1% idle condition.

Simulated landing-takeoff cycle emissions of configuration 12 were evaluated against current regulatory guidelines. Eq. (3) yields mass of NO_x emitted over a regulatory reference LTO cycle divided by rated engine

output. EI and \dot{m}_f correspond to the emission index for NO_x (g/kg) and liquid fuel mass flow rate (kg/min), respectively, at each subscript power setting. The maximum rated thrust is specified in kilonewtons. Table 7 contains the specific engine conditions and computed $EINO_x$ for configuration 12 at each of the four regulated LTO conditions.

From off-design results, the LTO NO_x per kilonewton thrust for the full annular combustor was determined from Eq. (4) to be 5.0. For the class engine analyzed in this study, the Civil Aviation Environmental Protection Tier 8 (CAEP/8) regulatory standard for LTO NO_x is given by Eq. (5) where represents the overall engine pressure ratio at sea-level takeoff.

$$LTO\ NO_x = \frac{0.7(EI \times \dot{m}_f) + 2.2(EI \times \dot{m}_f) + 4.0(EI \times \dot{m}_f) + 26.0(EI \times \dot{m}_f)}{\text{Maximum Rated Thrust}} \quad (4)$$

$LTO\ NO_x$

=

TABLE 7: LTO Cycle Emission Performance			
Power Setting (%)	\dot{m}_f (kg/min)	$EINO_x$ (g/kg)	Thrust (kN)
100	40.5	9.45	106.17
85	33.72	3.01	90.25
30	10.8	0.71	31.85
7.1	3.96	0.08	7.5

$$LTO\ NO_x = -9.88 + 2.0 \times OPR \quad (5)$$

Using the CAEP/8 guideline, the LTO NO_x regulation for a 33.1 OPR (at sea level) engine is 56.32-g/kN. Configuration 12 achieves over a 90% predicted $EINO_x$ margin below the CAEP/8 standard. Reviewing the

predicted emission indices at low power, the computed LTO NO_x is considered optimistic. While benefits are expected due to an advanced engine cycle with reduced liner cooling, some computational concerns exist. Potential factors contributing to EINO_x under-prediction at low power include use of a finite-rate chemistry mechanism, lack

of turbulence chemistry interaction and use of a steady-state simulation to predict a potentially unsteady spray break-up process. In addition, the reduced chemistry developed for computational efficiency was optimized for NO and CO prediction at pressures above the 7.1 and 30% power conditions. Lastly, combustion efficiency was observed to decline at low power conditions, meaning CFD computed exit temperatures were up to 2% below the adiabatic flame exit temperatures assumed by the NPSS cycle model. This indicates a subtle mismatch between the f/a assumed from cycle analysis and the actual f/a required to achieve the desired cycle T_4 temperature. While these factors are more negligible for high power simulations, they introduce a particular challenge for low power emission prediction. Despite computational concerns, the qualitative emission trends are considered feasible for concept definition based on past validation studies [28] and indicate more detailed modeling is needed to graduate the configuration to preliminary design.

VI. Conclusions

Next-generation low-emission aviation combustion calls for physics-based analysis tools to rapidly explore and characterize revolutionary fuel injection strategies and combustor layouts. This research proposes an integrated approach where new design spaces can be readily surveyed by directly coupling engine cycle analysis with multi-phase reacting CFD. For demonstration, design exploration of a candidate LDI-capable combustor for a small core ultra high bypass engine application was the subject of this study. The concept also leveraged radial fuel staging with an axial pilot dome offset, techniques intended to improve operability at low power conditions.

Qualitative and quantitative assessment of the annular radially staged combustor sector was performed, indicating sensitivity of geometric design parameters to combustor NO_x emissions and performance. Qualitative trends indicate combustor pressure loss is largely governed by air swirler vane angle. In general, designs with steep axial vanes (higher swirl numbers) displayed a reduced effective flow area, higher turbulent kinetic energy levels and more significant losses in total pressure. The pilot dome offset distance was found to weakly correlate with total combustor exit pressure loss through viscous effects. Pilot recirculation zone strength and size was observed to qualitatively increase with pilot dome offset. No detrimental impact to EINO_x was observed as a result of larger pilot dome recession at the full power condition. This suggests improved operability can likely be obtained by recessing pilot injectors without compromising emission performance at full power. Increasing flow-turning angle in the venturi reduced axial velocities and was found favorable to recirculation zone formation. Expanded pilot venturi exit areas were observed to promote recirculation zone volume and strength, ideal characteristics for stable low power lean operation. However, NO production qualitatively trended with recirculation zone uniformity between the pilot and main injector zones. Larger pilot injectors were found to produce significantly lower NO concentrations than main 1 and 2 injectors at full power and with assumed equal fuel splits. A sparse Pareto frontier was identified from the design space, highlighting a trade-off opportunity between EINO_x and combustor pressure loss. Generally, EINO_x improvements were found to compromise total pressure in the combustor and vice-versa.

Future opportunities exist for concept refinement and coupled combustor/engine cycle improvements. In particular, accurate low power emission prediction contains a number of challenges yet to be addressed.

Given the current design space exploration, low-order semi-analytical models may be constructed to help refine the Pareto front and simultaneously guide global search algorithms to identify other optimal configurations. Additionally, semi-analytical combustor models could be coupled directly into an engine cycle and used for rapid combustor/cycle optimization. Pros to this approach include more efficient system-level optimization capabilities, with the caveat of potential fitting errors introduced during semi-analytical model construction.

VII. Acknowledgements

The author gratefully acknowledges the Commercial Supersonic Technology and AeroSciences Projects of the NASA Fundamental Aeronautics Program for research funding. Acknowledgment is also due to Phil Lee of Woodward FST, Inc. for providing general injector design guidelines and Thomas Wey of NASA GRC for technical OpenNCC solver support.

References

- [1] Tacina, R., Lee, P., and Wey, C., "A Lean-Direct-Injection Combustor using a 9 Point Swirl-Venturi Fuel Injector," ISABE Paper 2005-1106, Munich, Germany, 2005.
- [2] Tacina, R., Wey, C., Laing, P., and Mansour, A., "Sector Tests of a Low-NO_x, Lean Direct Injection, Multipoint Integrated Module Combustor Concept," ASME Paper GT-2002-30089, pp. 533-544, Amsterdam, The Netherlands, 2002.
- [3] Lefebvre, A. H., "Gas Turbine Combustion," 2nd Ed., Taylor and Francis, pp. 23, Philadelphia, PA, 1999.
- [4] Heath, Christopher M. "Characterization of Swirl-Venturi Lean Direct Injection Designs for Aviation Gas Turbine Combustion," *Journal of Propulsion and Power*, (2014), accessed September 11, 2014, doi: <http://arc.aiaa.org/doi/abs/10.2514/1.B35077>
- [5] Claus, R. W., Evans, A. L., Follen, G. J., "Multidisciplinary Propulsion Simulation Using NPSS," AIAA Paper No. 92-4709-CP, 1992.
- [6] Lytle, J. K., "The Numerical Propulsion System Simulation: A Multidisciplinary Design System for Aerospace Vehicles," NASA/TM—1999-209194, 1999.
- [7] Mongia, H. C., "A Synopsis of Gas Turbine Combustor Design Methodology Evolution of Last 25 Years," Paper No. ISABE-2001-1086, Bangalore, India, 2001.
- [8] Mongia, H. C., "Aero-Thermal Design and Analysis of Gas Turbine Combustion Systems: Current Status and Future Direction," AIAA Paper No. 98-3982, 1998.
- [9] Heath, C., Hicks, Y., Anderson, R., and Locke, R., "Optical Characterization of a Multipoint Lean Direct Injector for Gas Turbine Combustors: Velocity and Fuel Drop Size Measurements," *Proceedings of ASME Turbo Expo 2010: Power for Land, Sea and Air Volume 2: Combustion, Fuels and Emissions, Parts A and B*, ASME, New York, 2010, pp. 791-802.
- [10] Dewanji, D. G., Rao, A. G., Pourquie, M., and van Buijtenen, J. P., "Investigation of Flow Characteristics in Lean Direct Injection Combustors," *Journal of Propulsion and Power*, Vol. 28, No. 1, 2012, pp. 181-196. doi:10.2514/1.B34264
- [11] Fu, Y., "Aerodynamics and Combustion of Axial Swirlers," Ph.D. Dissertation, Department of Aerospace Engineering and Engineering Mechanics, University of Cincinnati, Cincinnati, OH, 2008.
- [12] Montgomery, D. C., "Randomizes Blocks, Latin Squares, and Related Designs," *Design and Analysis of Experiments*, 6th ed., Wiley, Hoboken, 2005, pp. 136-142.
- [13] Ajmani, K., Kundu, K. P., Yungser S. J., "Assessment of Reduced-Kinetics Mechanisms For Combustion of Jet Fuel in CFD Applications," AIAA Paper No. 2014-3662, 50th AIAA/ASME/SAE/ASEE Joint Propulsion Conference and Exhibit, July 28-30, 2014, Cleveland, OH.
- [14] NASA, "NPSS User Guide: Rev. 1.6.5," Cleveland, OH, 12 March 2008.
- [15] Stubbs, R. M., and Liu, N.-S., "Preview of the National Combustion Code," AIAA Paper 1997-3114, 1997.
- [16] Chen, K.-H., Norris, A. T., Quealy, A., and Liu, N.-S., "Benchmarking Test Cases for the National Combustion Code," AIAA Paper 1998-3855, 1998.
- [17] Swanson, R.C., and Turkel, E., "Multistage Schemes with Mutigrid for Euler and Navier-Stokes Equations," NASA/TP—3631, 1997.
- [18] Ajmani, K., and Breisacher, K. J., "Computational Modeling of Discrete-Jet and Lean Direct Injectors," 48th AIAA/ASME/SAE/ASEE Joint Propulsion Conference and Exhibit, AIAA Paper 2012-4270. July-Aug. 2012.
- [19] Shih, T.-H., Chen, K.-H., and Liu, N.-S., "A Non-Linear k-epsilon Model for Turbulent Shear Flows," AIAA Paper 1998-3983, 1998.
- [20] Ajmani, K., Mongia, H., and Lee, P., "Evaluation of CFD Best Practices for Combustor Design: Part 2: Reacting Flows," AIAA Paper 2013-1143, 2013.
- [21] Shih, T.-H., Povinelli, L. A., Liu, N.-S., and Chen, K.-H., "Generalized Wall Function for Complex Turbulent Flows," NASA/TM—2000-209936, Cleveland, OH, June 2000.
- [22] Iannetti, A. C., Liu, N.-S. and Davoudzadeh, F., "The Effect of Spray Initial Conditions on Heat Release and Emissions in LDI CFD Calculations," NASA/TM—2008-215422, Cleveland, OH, Oct. 2008.

[23] Iannetti, A. C., and Moder, J. P., “Comparing Spray Characteristics from Reynolds-Averaged Navier-Stokes (RANS) National Combustion Code (NCC) Calculations Against Experimental Data for a Turbulent Reacting Flow,” NASA/TM-2010-216735, Cleveland, OH, July 2010.

[24] Chen, K.-H., and Liu, N.-S., “Evaluation of a Nonlinear Turbulence Model Using Mixed Volume Unstructured Grids,” AIAA Paper 1998-0233, 1998.

[25] Liu, N.-S., Shih, T.-H. and Wey, C. T., “Numerical Simulations of Two-Phase Reacting Flow in a Single-Element Lean Direct Injection (LDI) Combustor Using NCC,” NASA/TM—2011-217031, Cleveland, OH, July 2011.

[26] Davoudzadeh, F., Liu, N.-S., and Moder, J.P., “Investigation of Swirling Air Flows Generated by Axial Swirlers in a Flame Tube,” Proceedings of ASME Turbo Expo 2006, Paper No. GT2006-91300, Barcelona, Spain (also NASA/TM—2006- 214252).

[27] Ajmani, K., Mongia, H. C. and Lee, P., “CFD Best Practices to Predict NO_x, CO and Lean Blowout for Combustor Design,” ASME IGTI Paper No. GT2013-95669, ASME Turbo Expo 2013, June 2013, San Antonio, TX.

[28] Ajmani, K, Mongia, H. C., Lee, P., “CFD Computations of Emissions for LDI-2 Combustors with Simplex and Airblast Injectors,” 50th AIAA Joint Propulsion Conference and Exhibit, AIAA Paper No. 2014-3529, July 28-30, 2014, Cleveland, OH.

[29] Raju, M. S., “LSPRAY-IV: A Lagrangian Spray Module,” NASA CR-2012-217294, Cleveland, OH, Feb. 2012.

[30] Zeldovich, Y. B., “The Oxidation of Nitrogen in Combustion and Explosions,” Acta Physicochimica, Vol. 21, No. 4, 1946, pp. 577-628.

[31] Fenimore, C. P., “Formation of Nitric Oxide in Premixed Hydrocarbon Flames,” Symposium (International) on Combustion, Vol. 13, No. 1, 1971, pp. 373-380.

[32] Gray, J. S., NASA OpenMDAO.org, <http://openmdao.org/> [retrieved 20 Jan. 2014].

Supplemental Materials:

Simulation Results for all 15 Combustor Configurations

Figures S1-S9 contain contour plots of critical flow field data with side view images extracted along the sector centerline. Axial images were extracted in 5-mm increments with the zero reference location at the pilot dome face. Configuration numbers and design parameters are listed above each image set.

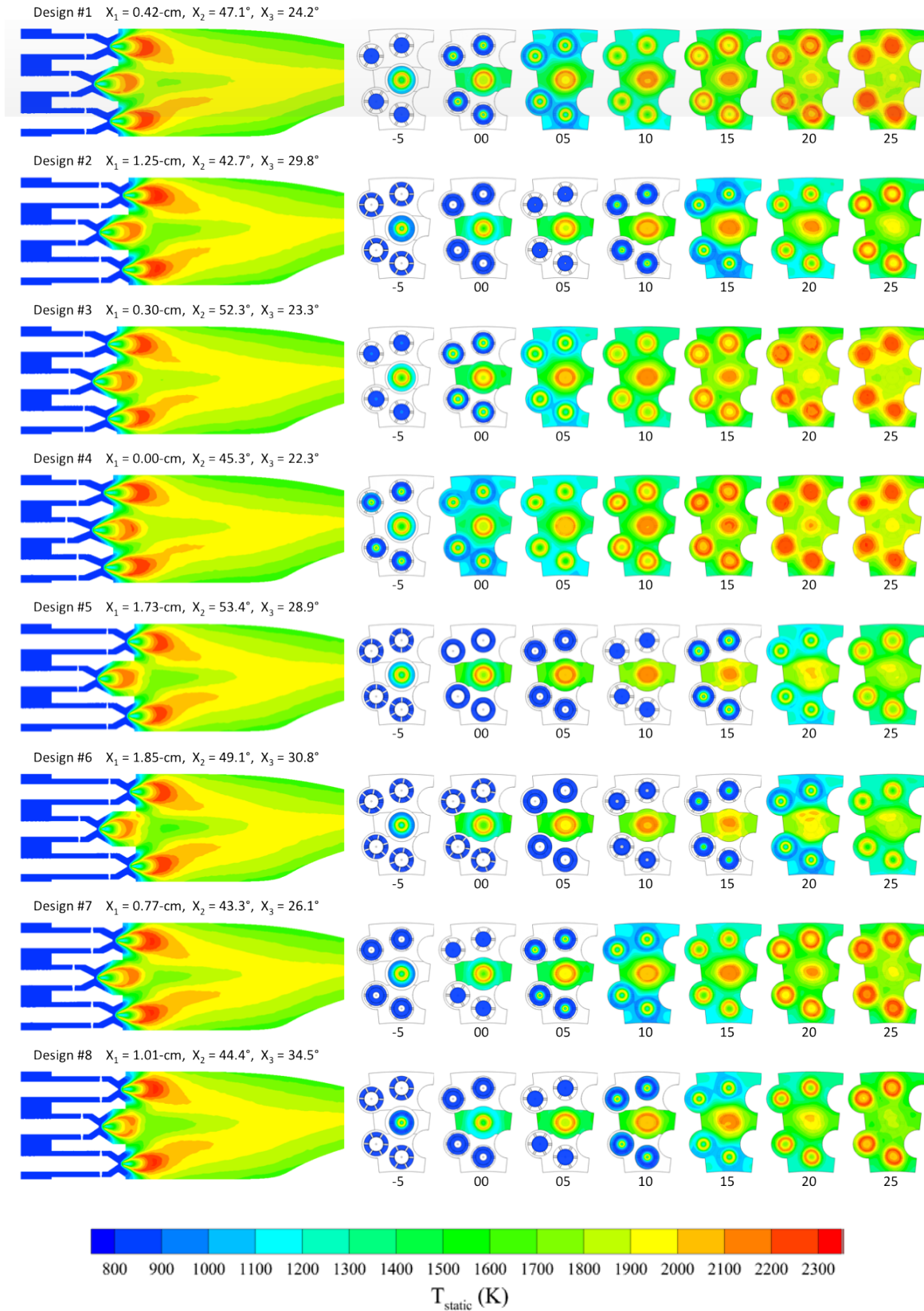


Fig. S1. Temperature contours for configurations 1-8. All designs exhibit stable attached flames. Pilot flame zones are typically reduced in size with more uniform local temperature fields.

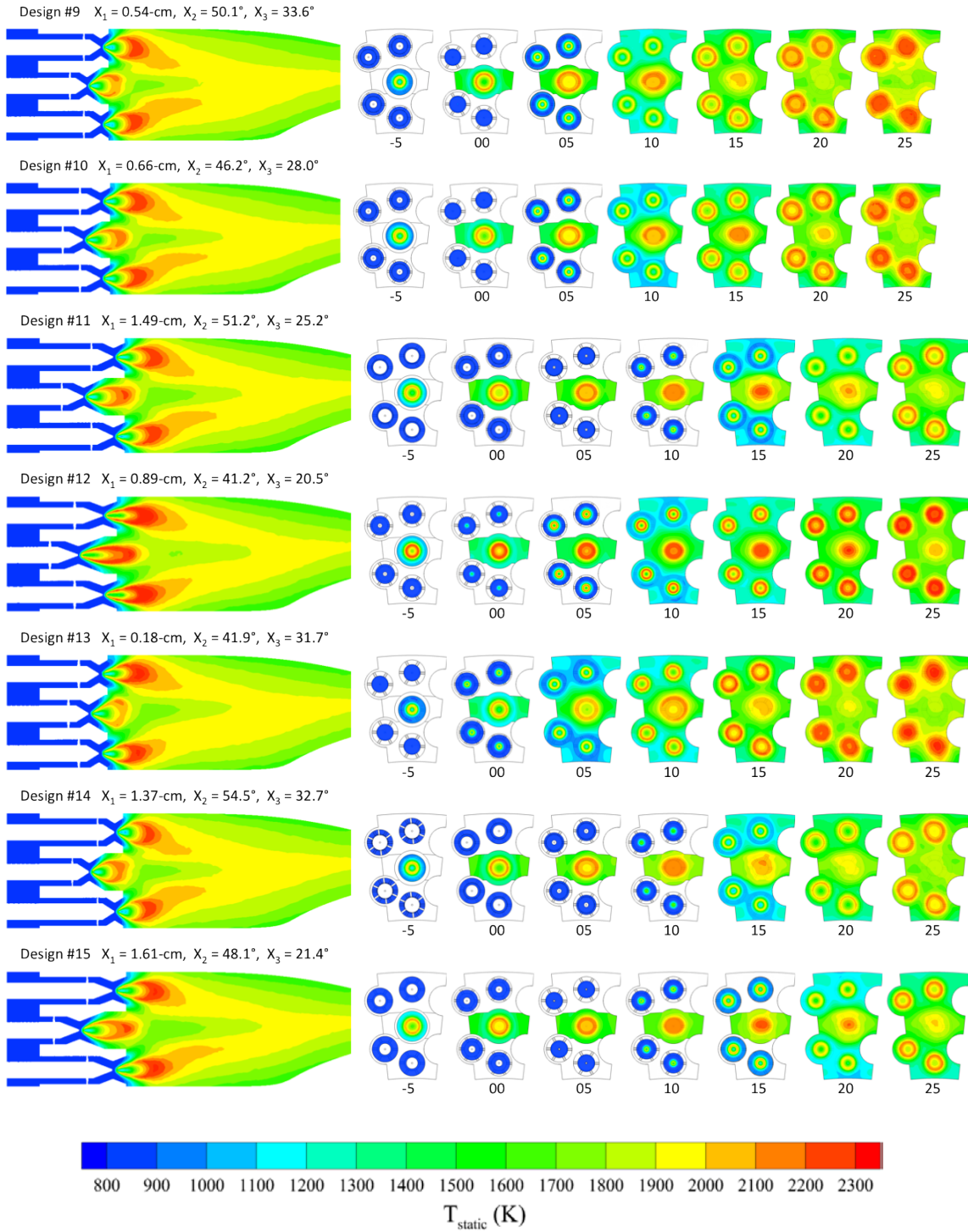


Fig. S2. Temperature contours for configurations 9-15. All designs exhibit stable attached flames. Pilot flame zones are typically reduced in size with more uniform local temperature fields.

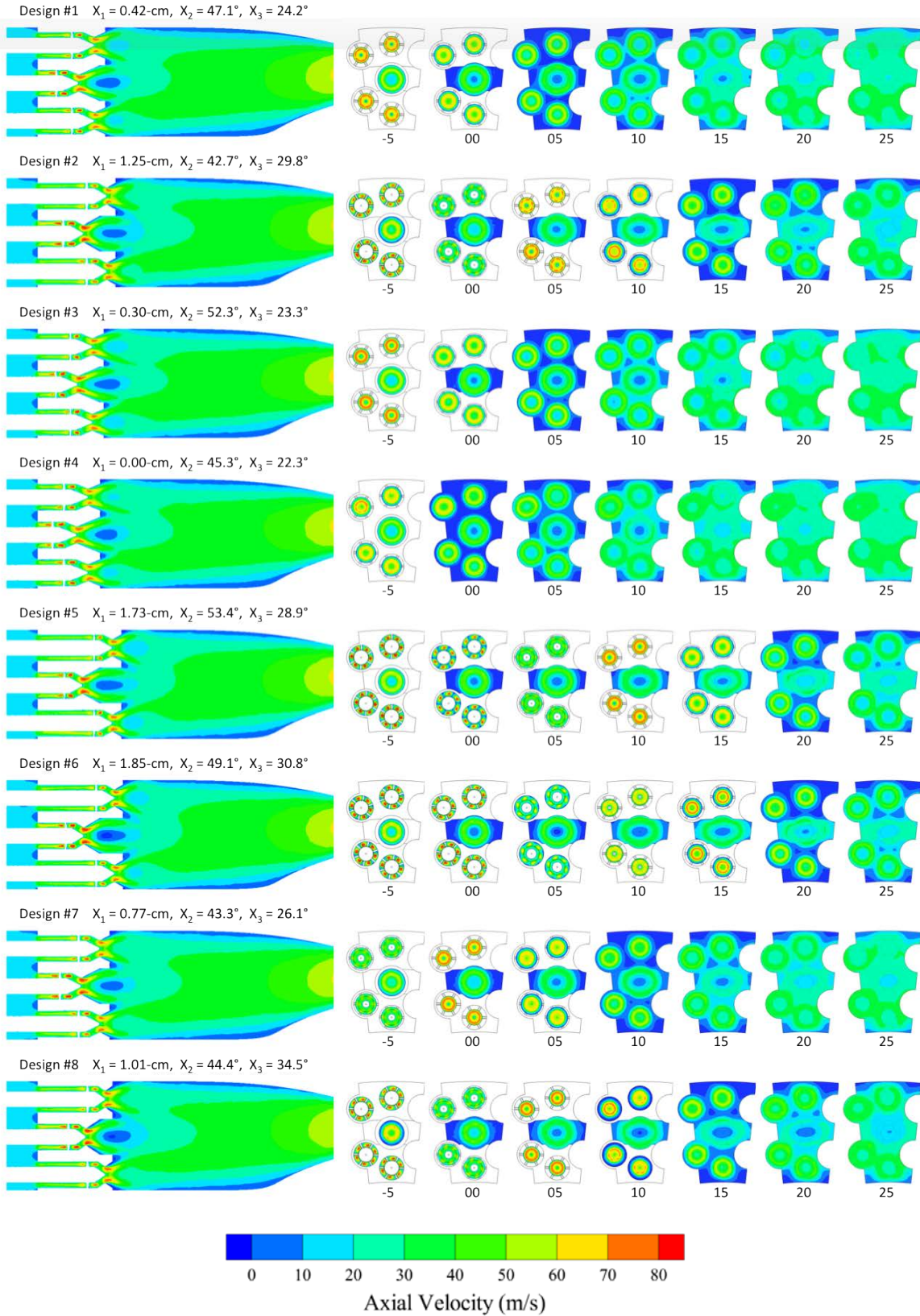


Fig. S3. Axial velocity contours for configurations 1-8. Pilot recirculation zone size/strength exceeds that of main injectors. Recirculation zone uniformity across injectors correlates with local NO mass fractions.

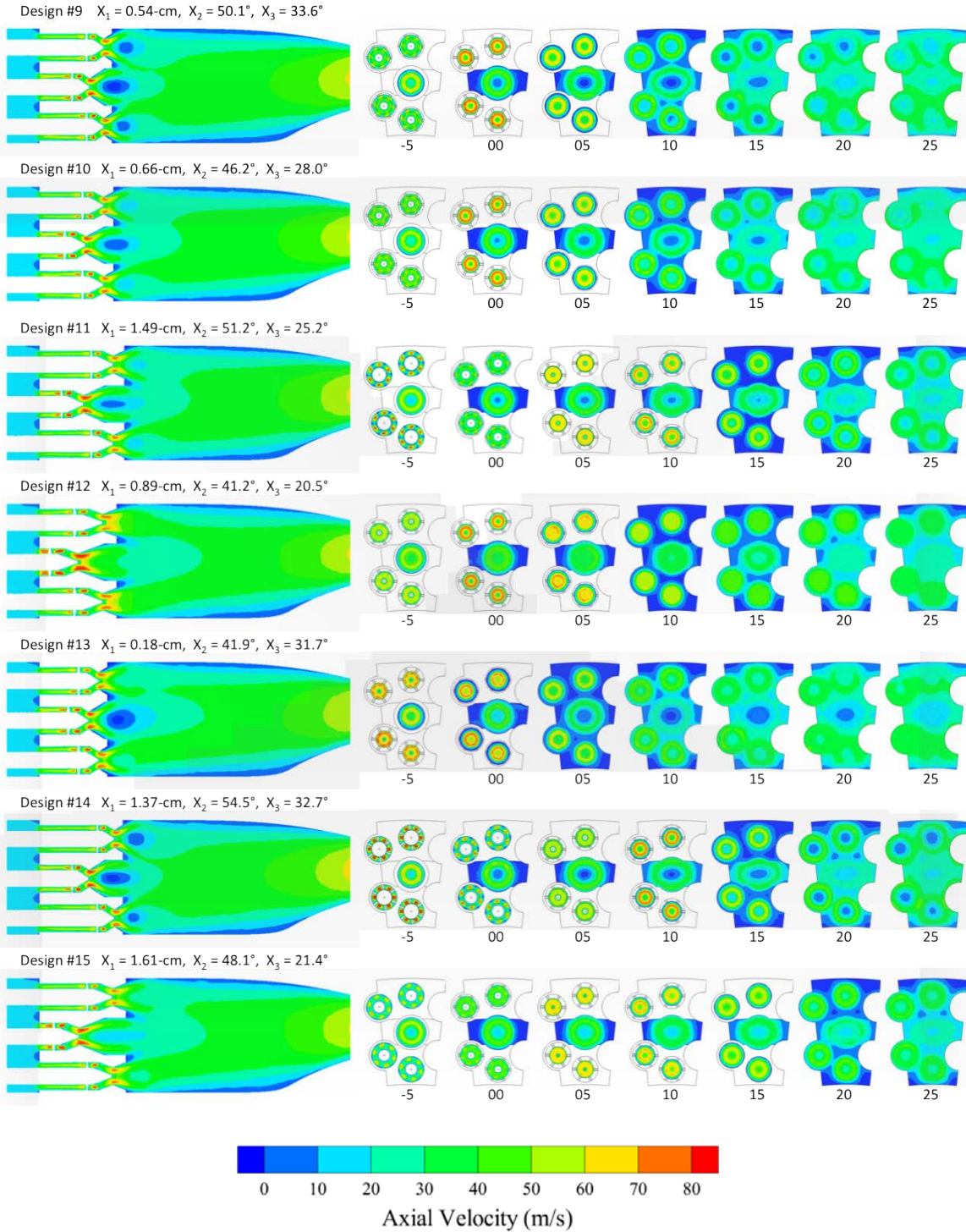


Fig. S4. Axial velocity contours for configurations 9-15. Pilot recirculation zone size/strength exceeds that of main injectors. Recirculation zone uniformity across injectors correlates with local NO mass fractions.

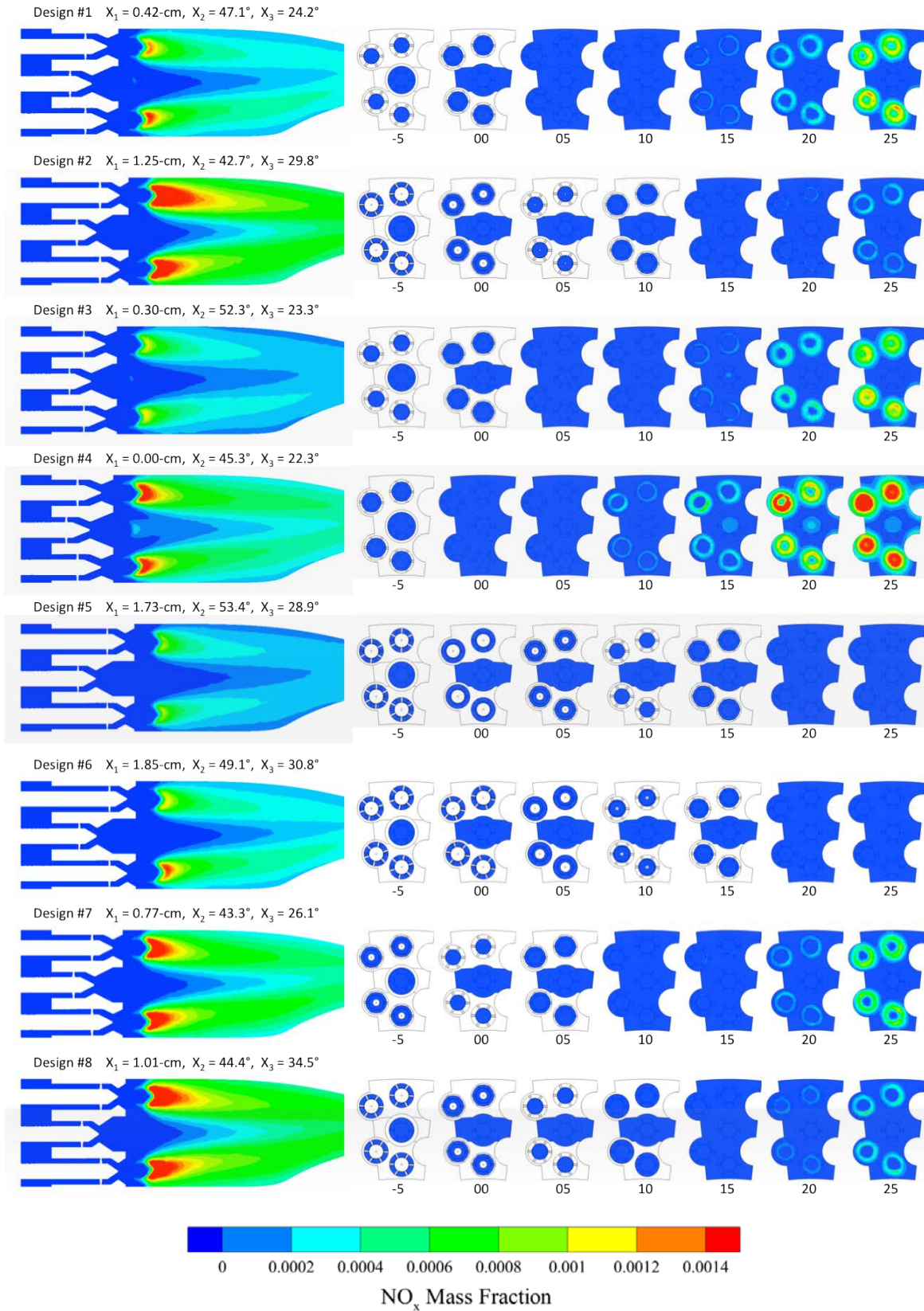


Fig. S5. NO species mass fraction contours for configurations 1-8. NO predominantly forms downstream of the burning zones and is substantially reduced near the pilot injector.

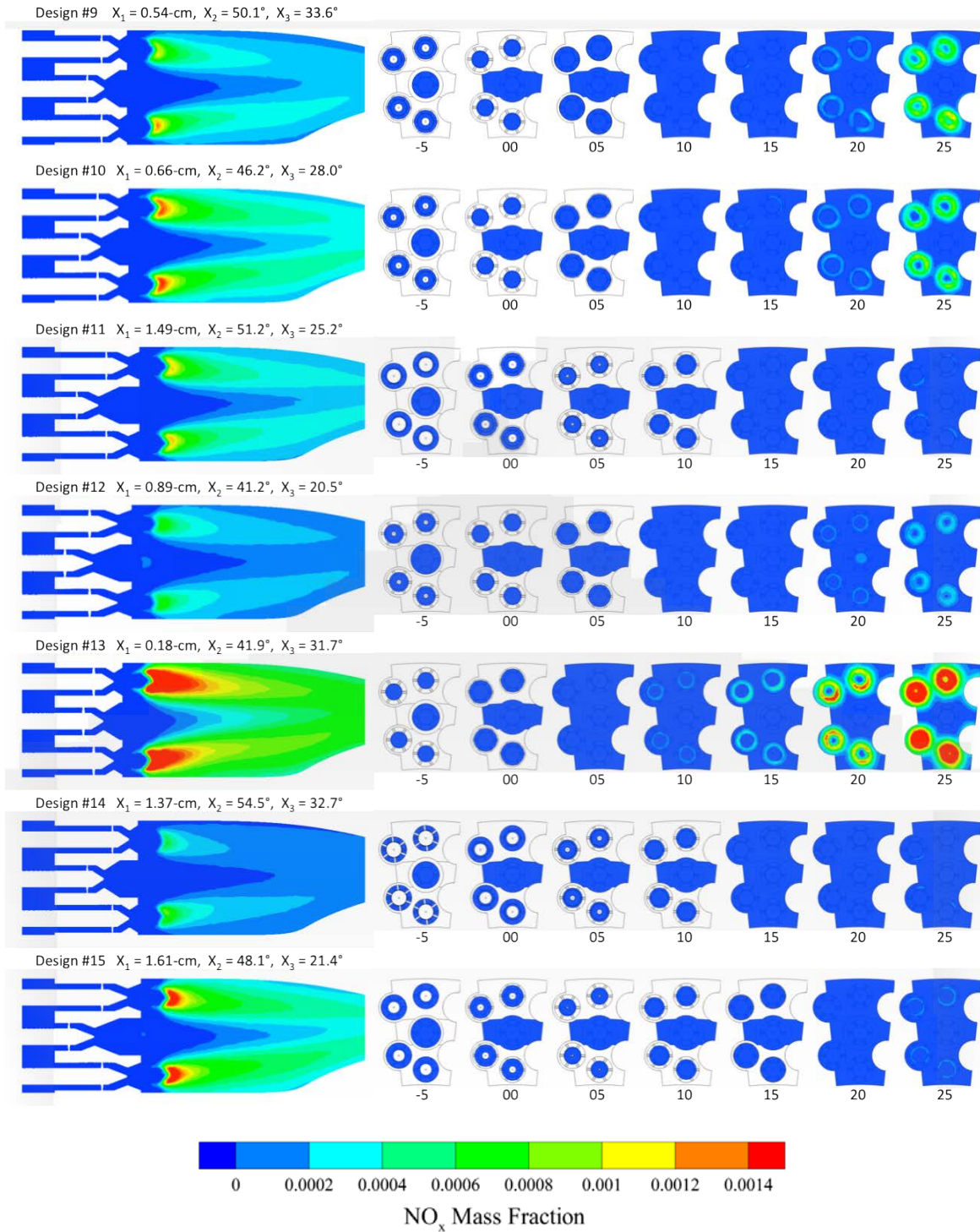


Fig. S6. NO_x species mass fraction contours for configurations 9-15. NO predominantly forms downstream of the burning zones and is substantially reduced near the pilot injector.

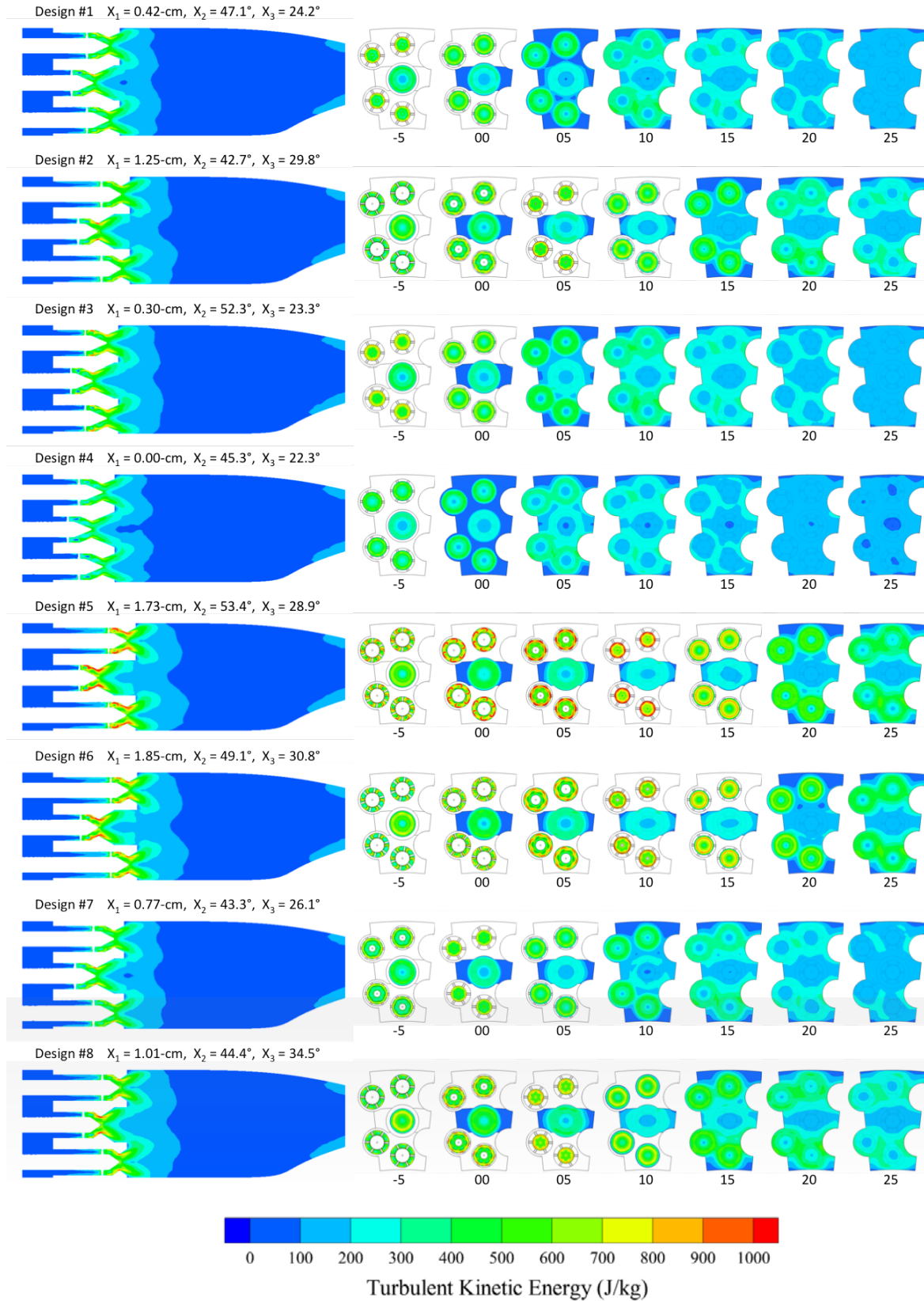


Fig. S7. Turbulent kinetic energy contours for configurations 1-8. Configurations with high TKE values in the vane passageway suffer largest overall pressure losses.

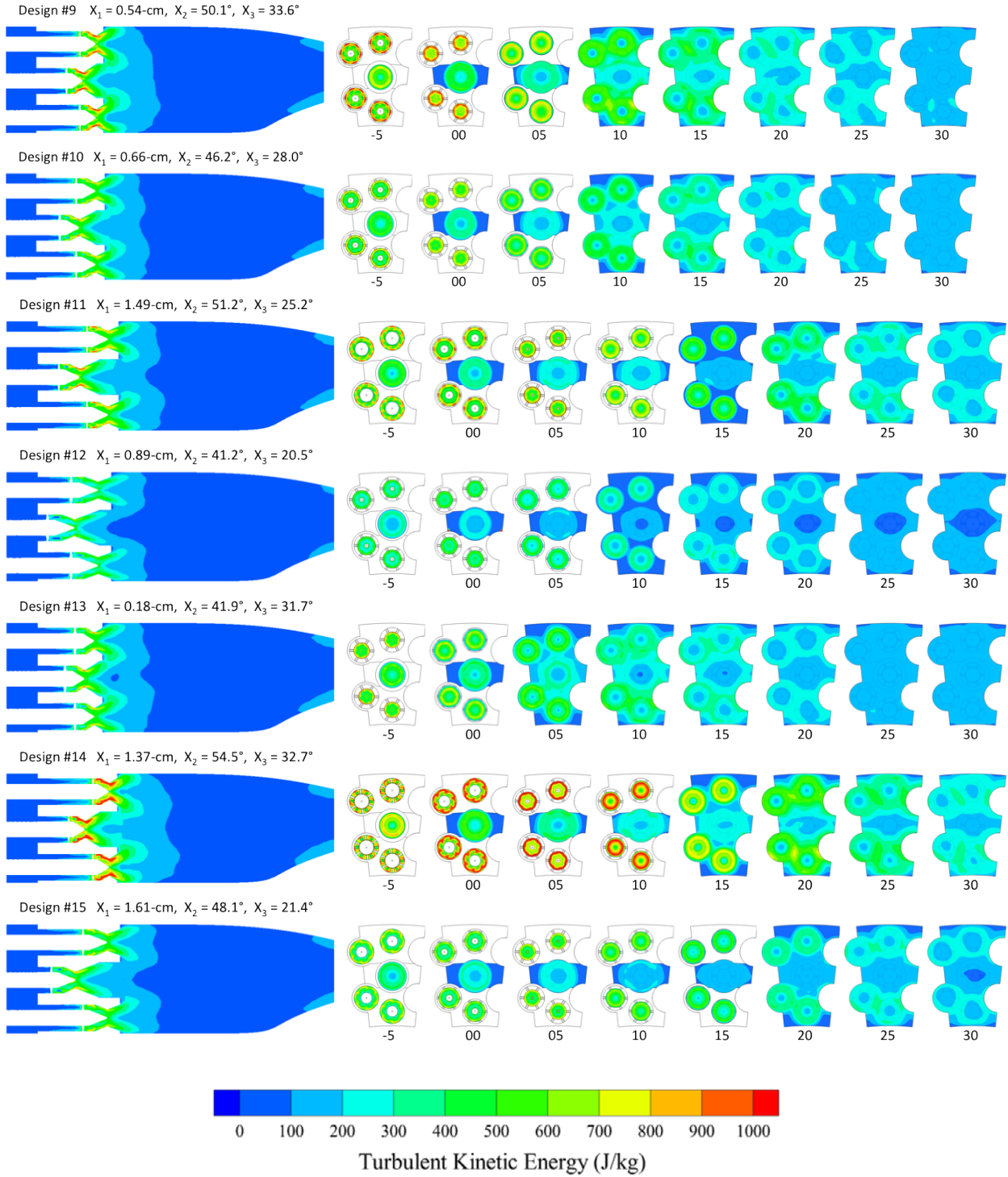


Fig. S8. Turbulent kinetic energy contours for configurations 9-15. Configurations with high TKE values in the vane passageway suffer largest overall pressure losses.

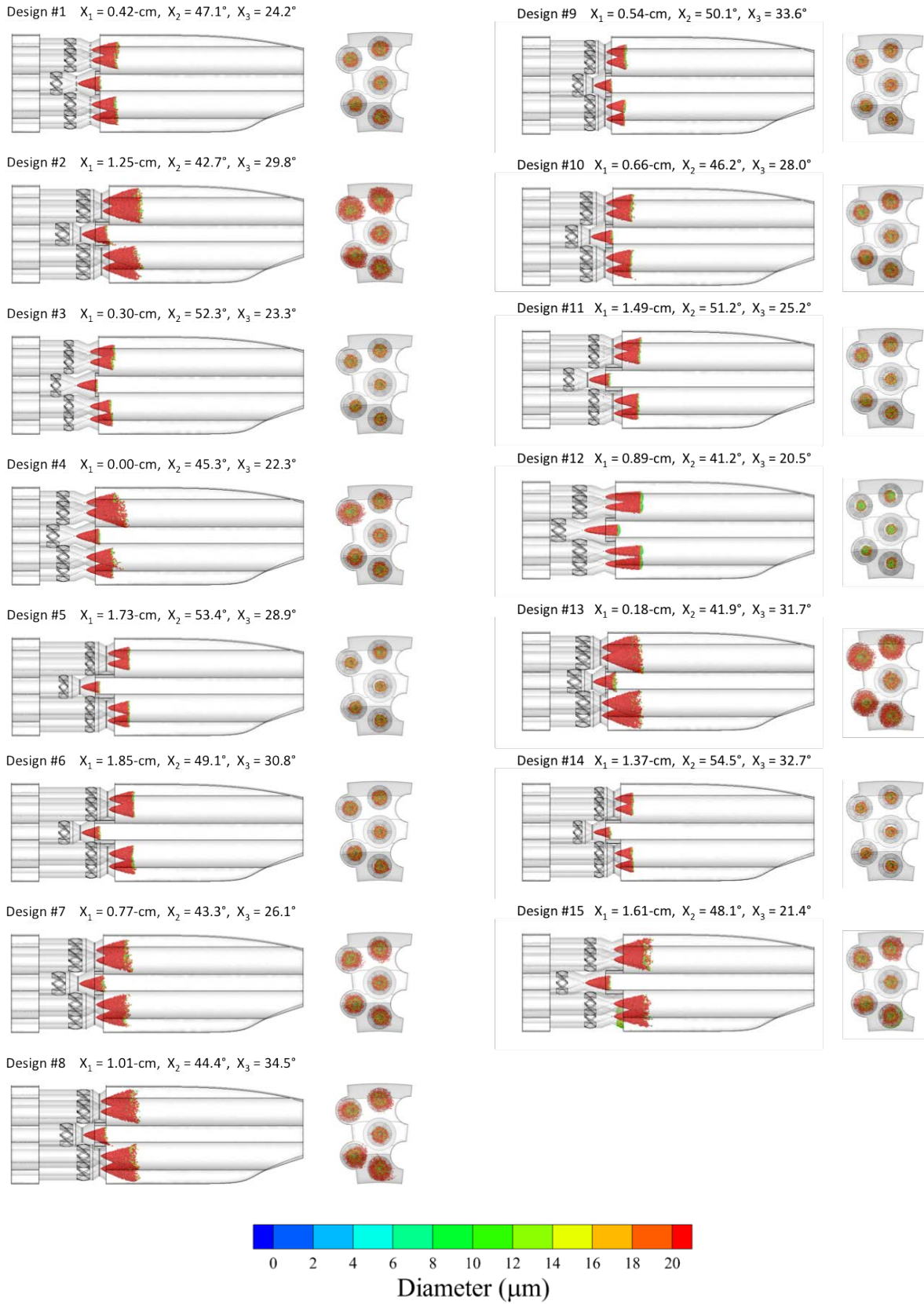


Fig. S9. Reacting liquid spray patters for all configurations. Designs with highest axial velocities near the injection sites exhibit reduced liquid spray cone patterns.